Two-dimensional topological effect in a transmon qubit array with tunable couplings

Yan-Jun Zhao,[1,*] Yu-Qi Wang,[1,†] Yang Xue,[2,3,†] Xun-Wei Xu,[4] Yan-Yang Zhang,[5] Wu-Ming Liu,[6,7] and Yu-xi Liu[2,3,‡]

[1]*Key Laboratory of Opto-electronic Technology, Ministry of Education, Beijing University of Technology, Beijing 100124, China*
[2]*School of integrated circuits, Tsinghua University, Beijing 100084, China*
[3]*Frontier Science Center for Quantum Information, Beijing 100084, China*
[4]*Key Laboratory of Low-Dimensional Quantum Structures and Quantum Control of Ministry of Education, Department of Physics and Synergetic Innovation Center for Quantum Effects and Applications, Hunan Normal University, Changsha 410081, China*
[5]*School of Physics and Materials Science, Guangzhou University, 510006 Guangzhou, China*
[6]*Beijing National Laboratory for Condensed Matter Physics, Institute of Physics, Chinese Academy of Sciences, Beijing 100190, China*
[7]*School of Physical Sciences, University of Chinese Academy of Sciences, Beijing 100190, China*

(Revised February 6, 2024)

We investigate a square-lattice architecture of superconducting transmon qubits with inter-qubit interactions mediated by inductive couplers. Therein, the inductive couling between the qubit and couplers is suggested to be designed into the gradiometer form to intigimate the flux noise orginating from the environment. Via periodically modulating the couplers, the Abelian gauge potential, termed effective magnetic flux, can be synthesized artificially, making the system an excellent platform for simulating two-dimensional topological physics. In the simplest two-dimensional model, the double (or three-leg) ladder, the staggered vortex-Meissner phase transition different from that in the two-leg ladder can be found in the single-particle ground state as the effective magnetic flux varies. Besides, the large coupling ratio between the interleg and intraleg coupling strengths also makes the chiral current resemble squeezed sinusoidal functions. If the row number is further increased, the topological band structure anticipated at massive rows begins to occur even for a relatively small number of rows (ten or so for the considered parameters). This heralds a small circuit scale to observe the topological band. The edge state in the band gap is determined by the topological Chern number and can be calculated through integrating the Berry curvature with respect to the first Brillouin zone. Besides, we present a systematic method on how to measure the topological band structure based on time- and space-domain Frourier transformation of the wave function after properly excited. The result offers an avenue for simulating two-dimensional topological physics on the state-of-the-art superconducting quantum chips.

I. INTRODUCTION

In the recent years, a few pioneering works have emerged in superconducting quantum circuits [1] that focused on quantum error correction [2–4], quantum superemacy demonstration [5–7], and even quantum chemistry simulation [8–10]. Fundamentally, these significant achievements can be attributed to the upgrade of the integration level and lifetime of superconducting qubits. For example, the recent Zuchongzhi processor [6] has achieved as high as 66 functional qubits with a mean lifetime 30.6 microseconds in an architecture of tunable couplings and tunable frequencies. Besides, the morelate Eagle processor [11] has reached to date the maximum qubit number 117 in a different architecture from Zuchongzhi. On the other hand, adopting the tantalum material, the qubit has elevated the lifetime to the remarkable hundreds of microseconds [12, 13]. The state-of-the-art integration level and lifetime heralds the noisy intermediate-scale quatnum (NISQ) era [14, 15].

One typical application of near-term NISQ devices is known as condensed matter physics simulation. On this topic, there have been entensive proposals and experiments based on single or several qubits [16–27], and also multiple qubits [5, 28–32, 35–43]. However, most multiple-qubit studies focused on one-dimension chains [33–38, 43] or quasi-two-dimensional ladders [39–41], and true-two-dimensional lattices [30, 42] are less studied. Indeed, the integration level and lifetime of the NISQ device make it an excellent platform to conduct two-dimensional simulation of condensed matter physics. In particular, the multiple-qubit quantum bahavior therein is an appealing topic which merits further investigation. Thus, it makes great sense to study two-dimensional simulation of condensed matter physics.

As is well konwn, the quantum Hall effect is a renowned phenomenon in two-dimensional condensed matter physics. Characterized by the Harper Hamiltonian, this phenomenon features the electron moving in a square lattice penetrated by uniform magnetic fields [44, 45]. As has been shown, for neutral atoms in an optical lattice, the Harper Hamiltonian can be similarly synthesized with the artificial magnetic fields, which can be engineered via periodically modulating the onsite energy [46–48] or classically driving the atomic internel states [49]. Compared to cold atoms, superconducting qubits possess the convenience of tunablility and scalability. Besides, there is already the experimental implementation of a "one-dimensional" Harper Hamiltonian using interacted transmon qubits mediated by inductive couplers [35]. However, how to synthesize the Harper Hamiltonian using two-dimensional superconducting NISQ circuis needs to be ex-

* The authors contributed equally to the work.; zhao_yanjun@bjut.edu.cn
† The authors contributed equally to the work.
‡ yuxiliu@mail.tsinghua.edu.cn

haustively studied.

Meanwhile, we note that the artificial magnetic fields can be synthesized via periodically modulating the inductive couplers in a triangle unit of transmon qubits [36]. This inspires us to further apply the inductive couplers to a square array of transmon qubits and further engineer the Harper Hamiltonian. Although it has been claimed that the inductive couplers can be applied to demonstrate the fractional quantum Hall effect, where the triangle and square-lattice models are discussed, no concrete circuits that realize these models have therein be calculated in detail [42]. Simultaneously, the inductive coupler can perfectly switch off the inter-qubit couplings, thus effectively avoiding the problem of frequency crowding [50]. However, the similar feature is not discussed in other artificial-magnetic-field-synthesizing schemes based on the nonlinearity of Josephson junctions [30, 51], and not possessed in those based on fixed couplings with periodically-modulated onsite energy [40, 52].

In this paper, we propose to engineer the Harper Hamiltonian in a two-dimensional architecture based on interacting transmon qubits mediated by inductive couplers. To be concrete, we first investigate the double-ladder model (i.e., three-row Harper Hamiltonian), and find a novel vortex-Meissner "phase transition" different from the one in the two-leg ladder model. This phase transition is resulted from the competition between the coupling strengths and magnetic flux. Then, we study the variation of the topological band structure when the row number is increased. In this way, feasible qubit numbers can be suggested for simulating observable topological phenomena.

In Sec. II, we introduce the transmon architecture with inductive-coupler-mediated interactions, from which the Harper Hamiltonian can be further derived. In Sec. III, we discuss the vortex number and chiral current in the double-ladder model for different magnetic fluxes and coupling strengths. In Sec. V, we discuss the topological effect when the row number is increased beyond three. In Sec. V, we discuss the experiment details on how to generate the single-particle ground state and measure the chiral currents and topological energy bands. In Sec. VI, we summarize the results.

II. QUBIT ARCHITECTURE WITH INDUCTIVE COUPLERS

A. Circuit model

We investigate a square array of transmon qubits with inter-qubit interactions mediated by inductive couplers. As schematically shown in Fig. 1(a), each qubit (colored blue) at the site nm (concise abbreviation for n, m without causing any ambiguity) couples intermediately via the coupler (colored red) to its four nearest neighbours at sites $n'm' = n \pm 1, m$ and $n, m \pm 1$. In detail, the qubit is grounded via a wound wire that consists of four different inductive segments [see Figs. 1(b)], which can operate as an gradiometer aiming at eliminating the homogeneous electromagnetic noise. The wire is plugged out from the SQUID (superconducting quantum interference device) that constitutes the transmon qubit [see Fig. 1(c)]. The qubit frequency can be controlled through the magnetic flux piercing the SQUID and the excitation and measurement of the qubit are realized by the cross-shaped capacitor that couples to the driving field and readout resonator [61]. Likewise, the inductive loop of the coupler [see Fig. 1(d)] is also designed as a gradiometer to cancel the homogeneous electromagnetic noise. The tunability of the coupler is guaranteed by the externally applied magnetic flux.

To be more intuitive, we now simplify the concrete circuit in Fig. 1(a) into a more general schematic in Fig. 1(e). Because of the externally applied magnetic flux $\Phi_{nm;n'm'}$, the coupler junction between any qubit site nm and its nearest neighbour $n'm'$ can be identified with a linear inductor to the small quantum signal [62]. This implies that the indirect qubit interaction mediated by the coupler can be modelled by a linear inductor network that describes the interplay between the SQUID branch currents I_{nm} and $I_{n'm'}$ at nm and $n'm'$. Therein, the mutual inductance possesses the form

$$M_{nm;n'm'} = -\frac{M_0^2 \cos\left(\frac{2\pi}{\Phi_0}\Phi_{nm;n'm'}\right)}{L_{\mathrm{T}} + 2L_0 \cos\left(\frac{2\pi}{\Phi_0}\Phi_{nm;n'm'}\right)}, \tag{1}$$

and the self inductance in series is $L_{nm} = 4L_0 + \sum_{n'm'\in\mathbb{C}_{nm}} M_{nm;n'm'}$ at the site nm (see Appendix. A). Here, the symbol $\mathbb{C}_{nm}$ represents all the four nearest neighbours of the site nm, Φ_0 the magnetic flux quantum, $L_{\mathrm{T}} = \Phi_0/2\pi I_{\mathrm{c}}$ the junction inductance of the coupler, I_{c} the critical current of the coupler junction, M_0 the mutual inductance between the coupler loop and the qubit loop grounding the SQUID, and L_0 the self inductance of one inductive segment of the gradiometer-shaped coupling loop. We stress that the two-site symbol is invariant if we exchange the order of the site indices, e.g., $M_{nm;n'm'} = M_{nm;n'm'}$.

To perform the canonical quantization [63], we use the node flux Φ_{nm} ($\Phi^{(\mathrm{g})}_{nm}$) to represent the node flux between the SQUID and shunting capacitor (gradiometer-shaped grounding wire) at the site nm. Then, we can give the Lagrangian of the whole circuit, that is,

$$\begin{aligned} L = &\sum_{nm} \frac{C\dot{\Phi}_{nm}^2}{2} + E_{\mathrm{J},nm} \cos\left[\frac{2\pi}{\Phi_0}\left(\Phi_{nm} - \Phi^{(\mathrm{g})}_{nm}\right)\right] \\ &- \sum_{nm} \frac{L_{nm} I_{nm}^2}{2} + M_{nm;n+1,m} I_{nm} I_{n+1,m} \\ &- \sum_{nm} M_{nm;n,m+1} I_{nm} I_{n,m+1}, \end{aligned} \tag{2}$$

where the two terms in the first line respectively denote the capacitive and Josephson inductive energies, while the last two lines represent the inductive energy induced by the coupler and surrounding circuit. Besides, the magnetic flux $\Phi^{(\mathrm{g})}_{nm}$, which originates from the currents flowing through the SQUIDs at nm and all its four nearest neighbours, takes the form

$$\Phi^{(\mathrm{g})}_{nm} = L_{nm} I_{nm} + \sum_{n'm'\in\mathbb{C}_{nm}} M_{nm;n'm'} I_{n'm'}, \tag{3}$$

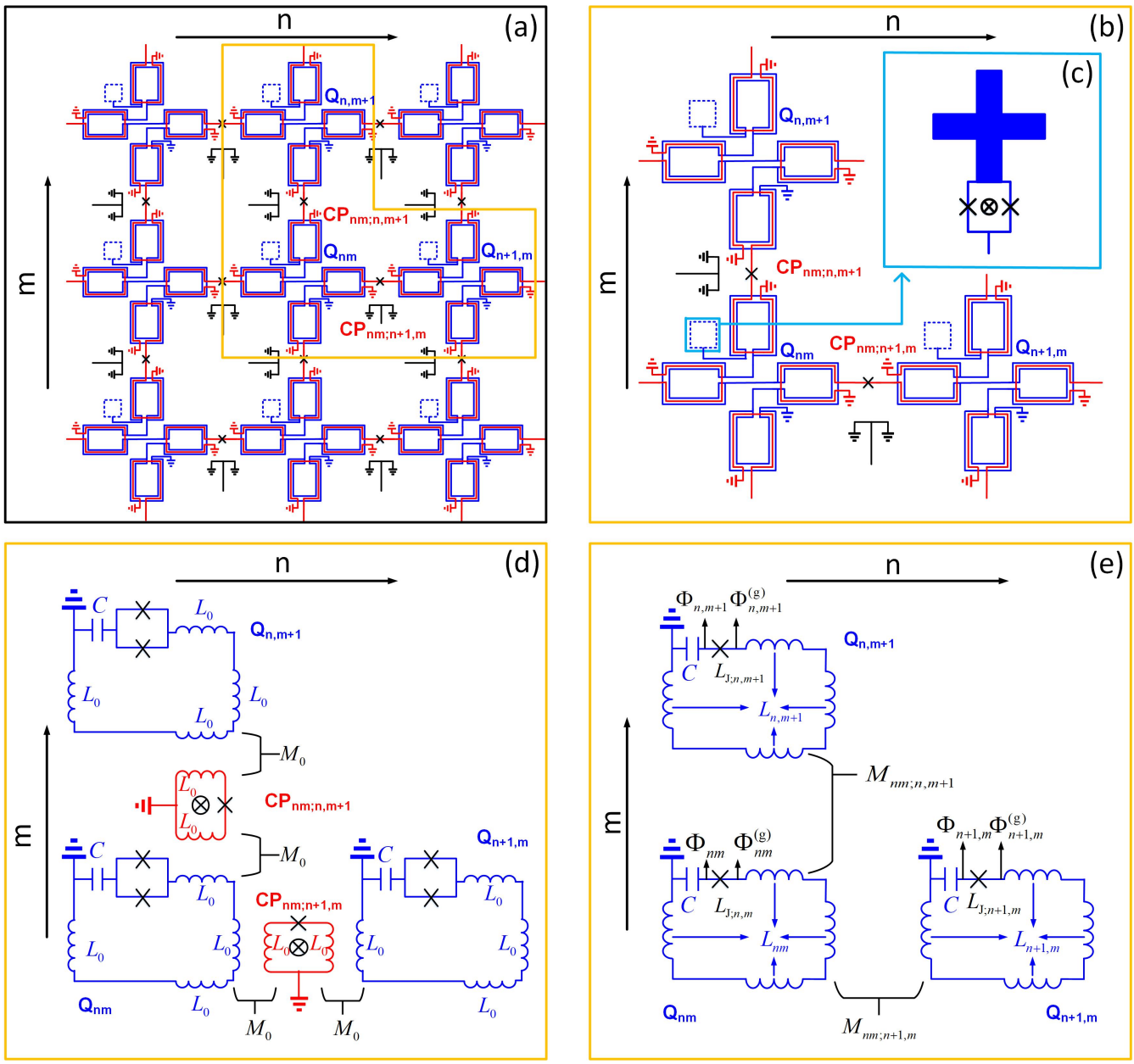

FIG. 1. (a) In the two-dimensional square lattice of transmons, the qubit at the site nm (denoted by Q_{nm} and colored blue) interacts with its nearest neighbours with an inductive coupler (colored red). Here, the horizontal and vertical coordinates, n and m, represent the column and row indices. The dashed blue squares denote the main part of qubit [see (c) for concrete structure]. (b) The coupling details between the qubit at nm (Q_{nm}) and its right ($\mathrm{Q}_{n+1,m}$) and upper ($\mathrm{Q}_{n,m+1}$) nearest neighbours. The transmon qubit is grounded via a specially meandering wire that acts as a gradiometer to cancel the environmental magnetic flux noise, and through which, the qubit inductively couples to each adjacent coupler (e.g., $\mathrm{CP}_{nm;n+1,m}$ or $\mathrm{CP}_{nm;n,m+1}$). The coupler consists of a Josephson junction and is tunable via the bias magnetic flux. (c) Main part of the qubit: the SQUID constituting the transmon connects to the cross-shaped capacitor that grounds the transmon that couples to the driving and read-out signals [61]. (d) Equivalent circuit diagram of the coupling mechanism shown in (c). The SQUID is shunted via a self capacitance (C) and located in a loop with four segments of identical self inductances (L_0). Each segment simultaneously couples to the adjacent coupler with a mutual inductance M_0. And the coupling segment in the coupler also possesses a self inductance L_0. The coupler junction inductance is L_{T}. (e) Simplified circuit diagram from (d), where the SQUID (superconducting quantum interference device) is modelled as one single junction (with the junction inductance $L_{\mathrm{J},nm}$ for the site nm, which is tunable by external magnetic flux threaded the SQUID loop), and the coupler-mediated indirect qubit-qubit coupling is replaced by a tunable mutual inductive coupling (e.g., with the mutual inductance $M_{nm;n+1,m}$ between the site nm and $n, m+1$). The resulting total inductance around the qubit loop is L_{nm} at the site nm. See Appendix. A for details. To construct the Hamiltonian, the node fluxes Φ_{nm} and $\Phi_{nm}^{(\mathrm{g})}$ are chosen respectively at the two terminals of the qubit junction at the site nm.

where $\mathbb{C}_{nm}$ means all the four nearest neighbours of the site nm as mentioned. Additionally, C is the homogeneous transmon shunting capacitance, $E_{\mathrm{J},nm} = \left(\frac{\Phi_0}{2\pi}\right)^2 \frac{1}{L_{\mathrm{J},nm}}$ the Josephson energy, and $L_{\mathrm{J},nm} = \frac{\Phi_0}{2\pi I_{\mathrm{c};nm}}$ the equivalent junction inductance of the SQUID, which is regarded as one single junction [see Fig 1.(e)]. According to the canonical quantization, the node charge takes $Q_{nm} = \partial L/\partial\dot{\Phi}_{nm}$, and the full Hamiltonian can be given by $H = \sum_{nm} Q_{nm}\dot{\Phi}_{nm} - L$, yielding

$$\begin{aligned} H =& \sum_{nm} \frac{Q_{nm}^2}{2C} - E_{\mathrm{J},nm}\cos\left[\frac{2\pi}{\Phi_0}\left(\Phi_{nm} - \Phi_{nm}^{(\mathrm{g})}\right)\right] \\ &+ \sum_{nm} \frac{L_{nm}I_{nm}^2}{2} + M_{nm;n+1,m}I_{nm}I_{n+1,m} \\ &+ \sum_{nm} M_{nm;n,m+1}I_{nm}I_{n,m+1}. \end{aligned} \tag{4}$$

where we have used In the assumption that the coupling is sufficiently weak, there is $\left|\Phi_{nm}^{(\mathrm{g})}\right| \ll |\Phi_{nm}|$, and the cosine function in Eq. (4) can be expanded up to the first order with respect to $\Phi_{nm}^{(\mathrm{g})}$. Then, the full Hamiltonian in Eq. (4) can be transformed into

$$H = \sum_{nm} H_{nm} + U_{nm},$$

where H_{nm} is the free qubit Hamiltonian at the site nm, and U_{nm} the interaction Hamiltonian between the site nm and its right and upper nearest neighbours, that is,

$$H_{nm} = \frac{Q_{nm}^2}{2C} - E_{\mathrm{J},nm}\cos\left(\frac{2\pi}{\Phi_0}\Phi_{nm}\right) - \frac{L_{nm}I_{nm}^2}{2}, \tag{5}$$

$$U_{nm} = -M_{nm;n+1,m}I_{nm}I_{n+1,m} - M_{nm;n,m+1}I_{nm}I_{n,m+1}. \tag{6}$$

Note that while Eqs. (5) and (6) were obtained, we implicitly made the approximation $I_{nm} = I_{\mathrm{c},nm}\sin\left[\frac{2\pi}{\Phi_0}\left(\Phi_{nm} - \Phi_{nm}^{(\mathrm{g})}\right)\right] \approx I_{\mathrm{c},nm}\sin\left(\frac{2\pi}{\Phi_0}\Phi_{nm}\right)$.

In the transmon regime [56], the Josephson energy $E_{\mathrm{J},nm}$ is much larger than the charging energy $E_{\mathrm{C}} = e^2/2C$ (e.g., $E_{\mathrm{J},nm}/\ E_{\mathrm{C}} \sim 50$, and e being the elementary charge) characterizing the capacitive energy. And then the qubit circuit mimics a virtual particle well localized in the vicinity of the Josephson potential energy bottom: $|\Phi_{nm}| \ll \Phi_0$. Thus, we can expand the free qubit Hamiltonian to the quartic order, giving

$$H_{nm} = \frac{Q_{nm}^2}{2C} + \frac{\Phi_{nm}^2}{2L_{\mathrm{J},nm}} - \frac{1}{24}\frac{1}{L_{\mathrm{J},nm}}\left(\frac{2\pi}{\Phi_0}\right)^2\Phi_{nm}^4, \tag{7}$$

Here, the term $\frac{1}{2}L_{nm}I_{nm}^2$ has been neglected by the assumption $L_{nm} \ll L_{\mathrm{J},nm}$.

B. Derivation of the Harper model

Now, we represent the node flux Φ_{nm} and node charge Q_{nm} with bosonic annihilation and creation operators a_{nm} and $a_{nm}^\dagger$, i.e.,

$$\Phi_{nm} = \sqrt{\frac{\hbar Z_{nm}}{2}}\left(a_{nm} + a_{nm}^\dagger\right), \tag{8}$$

$$Q_{nm} = \sqrt{\frac{\hbar}{2Z_{nm}}}\frac{\left(a_{nm} - a_{nm}^\dagger\right)}{i}. \tag{9}$$

Here, the parameter $Z_{nm} = \sqrt{L_{\mathrm{J},nm}/C}$ is called as the qubit impedance. Substituting Eqs. (8) and (9) into Eq. (7), the free Hamiltonian is transformed into

$$H_{nm} = \hbar\omega_{nm}a_{nm}^\dagger a_{nm} - \frac{E_{\mathrm{C}}}{2}a_{nm}^{\dagger 2}a_{nm}^2, \tag{10}$$

where $\omega_{nm} = \omega_{\mathrm{p},nm} - E_{\mathrm{C}}/\hbar$ is the qubit frequency, $\omega_{\mathrm{p},nm} = 1/\sqrt{CL_{\mathrm{J},nm}} = \sqrt{8E_{\mathrm{C}}E_{\mathrm{J},nm}}/\hbar$ the Josephson plasma frequency, and only the number-conserving terms are kept. Due tot the nonlinearity E_{C}, the the transmon can also be represented as a two-level system.

Hereafter, we will mainly focus on the case of the single-particle excitation, which means the nonlinear term $a_{nm}^{\dagger 2}a_{nm}^2$ can be neglected in the free Hamiltonian, thus making Eq. (10) become

$$H_{nm} = \hbar\omega_{nm}a_{nm}^\dagger a_{nm}. \tag{11}$$

When treating interaction Hamiltonian U_{nm}, we neglect the nonlinear effect of the SQUID, thus simplifying the SQUID branch current into $I_{nm} = \Phi_{nm}/L_{\mathrm{J},nm}$. Based on this approximation, the interaction Hamiltonian becomes

$$\begin{aligned} U_{nm} =& \hbar G_{nm;n+1,m}a_{nm}\left(a_{n+1,m} + a_{n+1,m}^\dagger\right) + \mathrm{H.c.} \\ &+ \hbar G_{nm;n,m+1}a_{nm}\left(a_{n,m+1} + a_{n,m+1}^\dagger\right) + \mathrm{H.c.}, \end{aligned} \tag{12}$$

where the first (second) line denotes the row (column) couplings, and the coupling strength $G_{nm;n'm'}$ takes the expression

$$G_{nm;n'm'} = -\frac{M_{nm;n'm'}}{2}\frac{\omega_{\mathrm{p},nm}\omega_{\mathrm{p},n'm'}}{\sqrt{Z_{nm}Z_{n'm'}}}. \tag{13}$$

As a first step to engineer effective magnetic flux in the Harper model [44, 45], the qubit frequencies should be synthesized according to the parity of the row index m. To do this, we assume that the SQUID's equivalent junction inductance takes $L_{\mathrm{J},nm} \equiv L_{\mathrm{J,o}}$ ($L_{\mathrm{J},nm} \equiv L_{\mathrm{J,e}}$) for the odd and even m, which can be conveniently achieved via tuning the bias magnetic flux. This leads to a set of parity-dependent parameters, which can be summarized as $X_{nm} \equiv X_{\mathrm{o}}$ ($X_{nm} \equiv X_{\mathrm{e}}$) for the odd (even) m where X denotes ω (qubit frequency), ω_{p} (plasma frequency), and Z (qubit impedance). Then, the full free Hamiltonian can be rewritten as

$$\begin{aligned} H_0 =& \sum_{nm} H_{nm} \\ =& \sum_{\substack{n \\ m\ \text{odd}}} \hbar\omega_{\mathrm{o}}a_{nm}^\dagger a_{nm} + \sum_{\substack{n \\ m\ \text{even}}} \hbar\omega_{\mathrm{e}}a_{nm}^\dagger a_{nm}, \end{aligned} \tag{14}$$

Secondly, the row coupling strengths are designed to be identical. For this purpose, we also specify the static bias magnetic flux of the row coupler according to the parity of the row index m, i.e., $\Phi_{nm;n+1,m} \equiv \Phi_{\rm o}$ ($\Phi_{n,m;n+1,m} \equiv \Phi_{\rm e}$) for the odd (even) row index m. This further results in parity-dependent row coupling strengths, that is, $G_{nm;n+1,m} \equiv G_{\rm o}$ ($G_{nm;n+1,m} \equiv G_{\rm e}$) for the odd (even) m. This, however, does not necessarily mean $G_{\rm o} \neq G_{\rm e}$, since from Eqs. (1) and (13), the difference caused by $\omega_{\rm o}$ and $\omega_{\rm e}$ as well as $Z_{\rm o}$ and $Z_{\rm e}$ can in principle be compensated via properly tuning $\Phi_{\rm o}$ and $\Phi_{\rm e}$. Hence, the homogeneous row coupling strengths can be created as $G_{\rm o} = G_{\rm e} = -g_x$. After the rotating-wave approximation is made for the intra-row coupling terms, the full interaction Hamiltonian reduces to

$$\begin{aligned} U =& \sum_{nm} U_{nm} = -\sum_{nm} \hbar g_x a_{nm} a_{n+1,m}^{\dagger} + \text{H.c.} \\ &+ \sum_{nm} \hbar G_{nm;n,m+1} a_{nm} a_{n,m+1}^{\dagger} + \text{H.c.}. \end{aligned} \tag{15}$$

The other critical step to synthesize the effective magnetic flux is biasing each column coupler with both direct and alternating components, i.e.,

$$\Phi_{nm;n,m+1} = \bar{\Phi} + \Phi_{\rm eff} \cos\left(\Delta t + \tilde{\gamma}_{nm}\right). \tag{16}$$

Here, $\tilde{\gamma}_{nm} \equiv -n\gamma$ ($n\gamma$) for odd (even) m, and the modulation frequency matches the frequency difference between adjacent rows, i.e., $\Delta = \omega_{\rm o} - \omega_{\rm e} > 0$. Then, suppose $L_0 \ll L_{\rm T}$, the column coupling strength should take the form

$$G_{nm;n,m+1} = 2t_y \cos\left[\frac{2\pi\bar{\Phi}}{\Phi_0} + \frac{2\pi\Phi_{\rm eff}}{\Phi_0} \cos\left(\Delta t + \tilde{\gamma}_{nm}\right)\right], \tag{17}$$

with $t_y = M_0^2 \omega_{\rm p,o} \omega_{\rm p,e} / 4 L_{\rm T} \sqrt{Z_{\rm o} Z_{\rm e}}$ denoting the bare column coupling strength. Besides, we mention that $\omega_{\rm p,o}$ ($\omega_{\rm p,e}$) is namely $\omega_{{\rm p},nm}$ for the odd (even) m and simultaneously, $Z_{\rm p,o}$ ($Z_{\rm p,e}$) is Z_{nm} for the odd (even) m.

Now, we discuss the inter-qubit couplings via entering the interaction picture defined by $U_0 = \exp\left(-\frac{i}{\hbar} H_0 t\right)$. This gives the time-dependent interaction Hamiltonian $H_{\rm I} = U_0^{\dagger} U U_0$, which takes the explicit form

$$\begin{aligned} H_{\rm I} =& -\sum_{nm} \hbar g_x a_{nm} a_{n+1,m}^{\dagger} + \text{H.c.} \\ &+ \sum_{nm} \hbar G_{nm;n,m+1} Y_{nm}(t) + \text{H.c.}, \end{aligned} \tag{18}$$

with the symbol $Y_{nm}(t) = a_{nm} a_{n,m+1}^{\dagger} e^{i(\omega_{n,m+1} - \omega_{nm})t}$. Here, note that the column coupling strength can also be expanded into the Fourier series as

$$\begin{aligned} G_{nm;n,m+1} =& t_y \sum_{k=-\infty}^{\infty} i^k e^{ik(\Delta t + \tilde{\gamma}_{nm})} J_k\left(\frac{2\pi\Phi_{\rm eff}}{\Phi_0}\right) \\ &\times \left[e^{i\frac{2\pi\bar{\Phi}}{\Phi_0}} + (-1)^k e^{-i\frac{2\pi\bar{\Phi}}{\Phi_0}}\right], \end{aligned} \tag{19}$$

where $J_k(\cdot)$ stands for the kth Bessel function of the first kind. Therefore, only keeping the resonant terms, we can obtain the final interaction Hamiltonian

$$H_{\rm I} = \hbar \sum_{\substack{n=-N \\ m=-M}}^{\substack{N-1 \\ M-1}} \left[\left(g_y e^{i\gamma n} a_{n,m+1}^{\dagger} - g_x a_{n+1,m}^{\dagger}\right) a_{nm} + \text{H.c.}\right], \tag{20}$$

where $g_y = -2t_y \sin\left(\frac{2\pi\bar{\Phi}}{\Phi_0}\right) J_1\left(\frac{2\pi\Phi_{\rm eff}}{\Phi_0}\right)$ is the bare column coupling strength. Here, we have concretely specified the length (width) of the two-dimensional lattice $L = 2N + 1$ ($W = 2M + 1$). Equation (20) is similar to the Harper model [44, 45] describing the two-dimensional integer quantum Hall effect.

C. Quasimomentum-space Hamiltonian

In the limit of infinite length ($L = \infty$), the lattice-space Hamiltonian [see Eq. (20)] can be decomposed into the ones in the row-direction quasimomentum space. This is achieved by first making the Fourier transformation of the bosonic operator, i.e.,

$$a_{nm} = \frac{1}{\sqrt{L}} e^{i\gamma mn} \sum_{k_x} e^{ik_x n} b_{k_x,m}, \tag{21}$$

where $b_{k_x,m}$ is the collective annihilation operator at the row-direction quasimomentum k_x and column-direction location m. After this transformation, the Hamiltonian $H_{\rm I}$ is changed into $H_{\rm I} = \sum_{k_x} \tilde{H}(k_x)$ with the quasimomentum-space Hamiltonian

$$\begin{aligned} \tilde{H}(k_x) =& \sum_{m=-M}^{M} \hbar\varepsilon_{\gamma m + k_x} b_{k_x,m}^{\dagger} b_{k_x,m} \\ &+ \sum_{m=-M}^{M-1} \left(\hbar g_y b_{k_x,m+1}^{\dagger} b_{k_x,m} + \text{H.c.}\right). \end{aligned} \tag{22}$$

and the notation $\varepsilon_k = -2g_x \cos k$. Here, the coupling strengths are generally of the order $g_{x(y)} \sim 2\pi \times 4\,\text{MHz}$ [36].

III. DOUBLE-LADDER MODEL

A. Single-particle energy spectrum

Firstly, we focus on the special double-ladder model, i.e., the simplest two-dimensional Harper model with the lattice width taking $W = 3$. Then, from Eq. (22), the quasimomentum-space Hamiltonian can be represented in the concise form $\tilde{H}(k_x) = b_{k_x}^{\dagger} h(k_x) b_{k_x}$ where $b_{k_x} = (b_{k_x,-1}, b_{k_x,0}, b_{k_x,1})^{\intercal}$ is an operator vector and the single-particle Hamiltonian $h(k_x) = h_z(k_x) + h_x$ is a 3×3 matrix

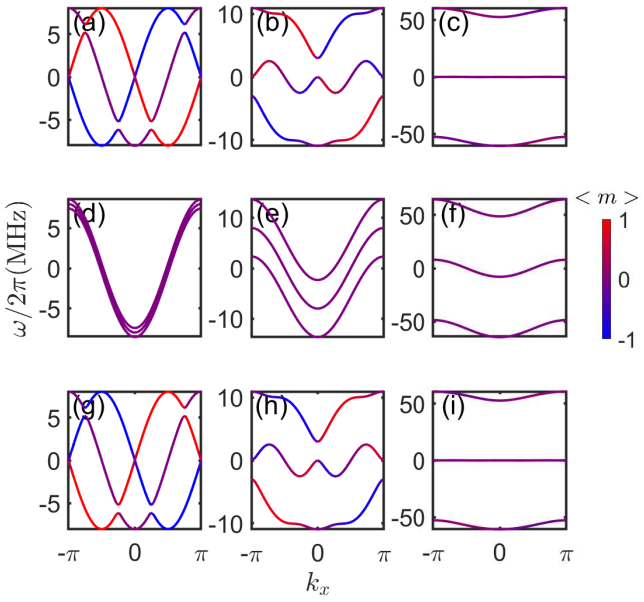

FIG. 2. (color online) Energy bands for the double-ladder model, i.e., the lattice width $W = 3$. Besides, the row coupling strength takes $g_x = 2\pi \times 4\,\mathrm{MHz}$ in all plots. However, in each column from leftmost to rightmost, the column coupling strength takes $g_y = 0.1g_x$, g_x, and $10g_x$, respectively. And in each row from top to bottom, the effective magnetic flux takes $\gamma = -\frac{\pi}{2}$, 0, and $\frac{\pi}{2}$, respectively. Furthermore, the curve color represents $\langle m \rangle$, i.e., the average location along the y direction in the present state.

with C

$$h_z\left(k_x\right) = \hbar \begin{pmatrix} \varepsilon_{k_x-\gamma} & 0 & 0 \\ 0 & \varepsilon_{k_x} & 0 \\ 0 & 0 & \varepsilon_{k_x+\gamma} \end{pmatrix}, \tag{23}$$

$$h_x = \hbar g_y \begin{pmatrix} 0 & 1 & 0 \\ 1 & 0 & 1 \\ 0 & 1 & 0 \end{pmatrix}. \tag{24}$$

Using the superscript $\intercal$ to denote the matrix transposition, the eigenvectors of h_z are then $e_{z,-1} = (1,0,0)^\intercal$, $e_{z,0} = (0,1,0)^\intercal$, and $e_{z,1} = (0,0,1)^\intercal$ with eigenvalues $E_{z,-1} = \hbar\varepsilon_{k_x-\gamma}$, $E_{z,0} = \hbar\varepsilon_{k_x}$, and $E_{z,1} = \hbar\varepsilon_{k_x+\gamma}$, respectively. However, an exception occurs for $\gamma = 0$, when $h_z = \hbar\varepsilon_{k_x} I$ with I being the identity matrix. The eigenvectors of h_x are $e_{x,-1} = \frac{1}{2}\left(1,-\sqrt{2},1\right)^\intercal$, $e_{x,0} = \frac{1}{2}\left(-\sqrt{2},0,\sqrt{2}\right)^\intercal$, and $e_{x,1} = \frac{1}{2}\left(1,\sqrt{2},1\right)^\intercal$ with eigenvalues $E_{x,-1} = -\sqrt{2}\hbar g_y$, $E_{x,0} = 0$, and $E_{x,1} = \sqrt{2}\hbar g_y$. The competition between h_z and h_x results in the energy bands shown in Fig. 2, where g_x is fixed at $2\pi \times 4\,\mathrm{MHz}$, but g_y and γ are varied.

For $\gamma = -\frac{\pi}{2}$ and $g_y = 0.1g_x$ [see Fig. 2(a)], the energy bands are mainly determined by h_z, which possesses three-branch eigenvalues $\hbar\varepsilon_{k_x-\gamma}$, $\hbar\varepsilon_{k_x}$, and $\hbar\varepsilon_{k_x+\gamma}$ corresponding to eigenvectors $e_{z,-1}$, $e_{z,0}$, and $e_{z,1}$. Under each vector, the average location along the column direction is accordingly $\langle m\rangle_{e_{z,-1}} = -1$, $\langle m\rangle_{e_{z,0}} = 0$ and $\langle m\rangle_{e_{z,1}} = 1$. In addition, the minimum points of these three branches are degenerate at $k_x = \gamma, 0$, and $-\gamma$, respectively. However, the presence of h_x makes these three branches hybridized, ending with a broken degeneracy. Then, the minimum value is actually only achieved at $k_x = 0$ [see Appendix. C]. When g_y is increased to g_x [see Fig. 2(b)], h_x becomes more important, the unique minimum at $k_x = 0$ can be figured out more apparently. When $g_y = 10g_x$ [see Fig. 2(c)], h_x nearly dominates the single-particle Hamiltonian. Under the eigenvectors of h_x, the average location along the column direction takes $\langle m\rangle_{e_{x,j}} = 0$ $(j = 1,2,3)$. The three energy bands become flatter, which are $E'_{x,-1} = -\sqrt{2}\hbar g_y + \frac{\hbar}{4}\varepsilon_{k_x-\gamma} + \frac{\hbar}{2}\varepsilon_{k_x} + \frac{\hbar}{4}\varepsilon_{k_x+\gamma}$, $E'_{x,0} = \frac{\hbar}{2}\varepsilon_{k_x-\gamma} + \frac{\hbar}{2}\varepsilon_{k_x+\gamma}$, and $E'_{x,1} = \sqrt{2}\hbar g_y + \frac{\hbar}{4}\varepsilon_{k_x-\gamma} + \frac{\hbar}{2}\varepsilon_{k_x} + \frac{\hbar}{4}\varepsilon_{k_x+\gamma}$ by the perturbative theory. Besides, there is still a unique minimum point which only occurs at $k_x = 0$.

When we change γ to 0, $h_z = \hbar\varepsilon_{k_x}$ is in fact a global shift to h_x. Since the eigenenergies of h_x are independent of k_x, the energy gaps maintain constant for changing k_x [see Figs. 2(d)-2(f)]. But there is a band bending when k_x varies, which is fundamentally induced by the function ε_{k_x}. When $g_y = 10g_x$, the bending becomes less obvious [see Fig. 2(f)] because h_x becomes dominant. The three bands still correspond to the eigenstates e_{xj} $(j = 1,2,3)$, under which, the average location along the column direction takes $\langle m\rangle_{e_{x,j}} = 0$ $(j = 1,2,3)$.

Next, we focus on the case $\gamma = \frac{\pi}{2}$, where the single-particle Hamiltonian $h_{k_x}|_{\gamma=\frac{\pi}{2}}$ can be easily proved to be equivalent to $h_{-k_x}|_{\gamma=-\frac{\pi}{2}}$ [see Eq. (24)]. Thus, the energy bands in Figs. 2(g)-2(i) can be obtained by symmetrizing Figs. 2(a)-2(c) with respect to the axis $k_x = 0$. Hence, we do not make further discussions for this case.

As has been discussed in cold atoms [49, 55], multiple fermions below the fermion energy can occupy both the edge states and the bulk states, thus exhibiting chiral dynamics. However, what the chiral dynamics like in the single-particle case remains to be investigated. Simultaneously, since the transmon qubits [see Eq. (10)] should be treated as two-level qubits beyond the single-particle case, the ordinary Jordan-Wigner transformation having successfully dealt with the one-dimensional qubit chain [58] proves ineffective in the two-dimensional qubit array [59]. Thus, priority to the multiple-particle scenario, the single-particle-ground-state chiral dynamics in the double ladder merits deep investigation.

B. Current pattern in the open-boundary condition

In the open-boundary condition, the continuous spectrum in Fig. 2 is discretized. We assume that the single-particle eigenstate regarding the energy level E_j $(j = 1,2,\cdots,WL$, and $E_1 \leq E_2 \cdots \leq E_{WL})$ is $|E_j\rangle = S_j^+|0\rangle$, where $|0\rangle$ is the (global) ground state and

$$S_j^+ = \sum_{n=-N}^{N}\sum_{m=-M}^{M} \psi_{nm}^{(j)} a_{nm}^\dagger \tag{25}$$

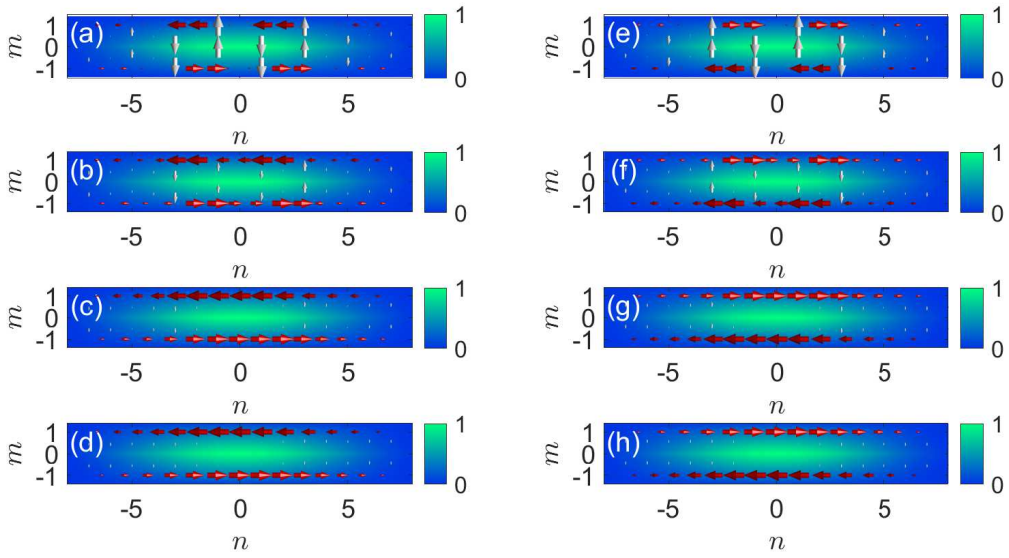

FIG. 3. (color online) Particle current patterns for the effective magnetic flux γ taking (a)-(c) $-\frac{\pi}{2}$ and (d)-(f) $\frac{\pi}{2}$ in a double ladder (lattice width $W = 3$) with the lattice length length $L = 17$. From top to bottom, the coupling strengths along two directions fulfill the conditions $K = 0.1$, 0.2, 0.4, and 0.7, respectively. The particle current between adjacent sites is represented by a arrow whose size implies the current magnitude. We have used the red (green) color for currents along the edge (in the bulk). Beside, the color in the background represents the relative occupation probability in the single-particle ground state. (See Fig. 11 in Appendix. B for normalized current patterns where the number of vortices can be counted more easily.)

is single-particle eigenstate creation operator. Particularly, the single-particle ground state is namely $|G\rangle = |E_1\rangle = S_1^+ |0\rangle$.

To characterize the current pattern in the single-particle ground state, we first seek $I_{nm;n'm'}$, the particle current operator from the site nm to $n'm'$, which, from the continuity equation

$$\frac{\mathrm{d}}{\mathrm{d}t}\left(a_{nm}^\dagger a_{nm}\right) = \frac{\left[a_{nm}^\dagger a_{nm}, H\right]}{i\hbar} = -\sum_{\text{adjacent } n'm'} I_{nm;n'm'} \tag{26}$$

can be derived to possess the general form as follows, that is,

$$I_{nm;n'm'} = -i\left(g_{nm;n'm'} a_{nm} a_{n'm'}^\dagger - \text{H.c.}\right). \tag{27}$$

Here, $g_{nm;n'm'}$ represents the coupling strength between the sites nm and $n'm'$ in the original Hamiltonian H [see Eq. (20)]. For example, for (n', m') taking $(n+1, m)$, $g_{nm;n'm'}$ is replaced with $-g_x$, while for (n', m') taking $(n, m+1)$, $g_{nm;n'm'}$ is replaced with $g_y e^{i\gamma n}$. In the state $|G\rangle$, the mean current from the site nm to $n'm'$ is then

$$\begin{aligned} I_{nm;n'm'}^{\mathrm{G}} &= \langle G| I_{nm;n'm'} |G\rangle \\ &= -i\left(g_{nm;n'm'} \psi_{nm}^{(1)} \psi_{n'm'}^{(1)*} - \text{c.c.}\right). \end{aligned} \tag{28}$$

Before intuitively showing the current patterns, we first introduce the concept of vortex, which represents a current pattern that all the particle currents circulate around a center either clockwise or anticlockwise. In Fig. 3, the current patterns have been plotted for different effective magnetic fluxes γ and coupling ratios $K = g_y/g_x$. For the case of $\gamma = -\pi/2$ [see Figs. 3(a)-(d)], we can see the vortices number continues to decrease, in detail, from 7, 4, 2, to 1, for K taking 0.1, 0.2, 0.4, and 0.7, respectively. In Fig. 3(d), the mere one vortices only appear on the edge, which we call the Meissner effect in analogue to the one in superconductor material. If the γ is flipped to $\pi/2$ [see Figs. 3(d)-3(f)], we see the particle currents only changes the directions for the same coupling strength ratio. This reveals the coupling ratio is critical to the vortex-Meissner phase transition. As illustrated by the background color in each panel, the bulk (i.e., the central row) is mostly populated compared to edges, which, however, does not induce a larger particle current from or to the central row sites, in that the particle current is additionally affected by the relative phase between adjacent sites.

For example, in Fig. 3, the particle current in the bulk, i.e., the central row, is always zero. This can be explained by investigating the property of the single-particle ground state $\psi_{nm}^{(1)} \equiv \psi_{nm}^{(1)}(\gamma)$. To do this, we first consider the case of broken time-reversal symmetry ($\gamma \neq 0, \pm\pi$). Then we rotate the double ladder by π with respect the axis $m = 0$, after which, the Hamiltonian $H_{\mathrm{I}} \equiv H_{\mathrm{I}}(\gamma)$ and wave function $\psi_{nm}^{(1)}(\gamma)$ respectively become $H_{\mathrm{I}}(-\gamma)$ and $\psi_{n,-m}^{(1)}(\gamma)$, where the relation $H_{\mathrm{I}}(-\gamma) = E_1 \psi_{n,-m}^{(1)}(\gamma)$ must hold. On the other hand, we note $H_{\mathrm{I}}(-\gamma)$ can also be obtained by taking the time-reversal of $H_{\mathrm{I}}(\gamma)$ and the eigenstate of $H_{\mathrm{I}}(-\gamma)$ with the eigen energy E_1 should be equivalent to $\psi_{n,m}^{(1)*}(\gamma)$ (see Appendix. C). Thus, via a well-chosen gauge, we can simply

think $\psi^{(1)*}_{n,m}(\gamma) \equiv \psi^{(1)}_{n,-m}(\gamma)$, which further gives $\psi^{(1)*}_{n,0}(\gamma) \equiv \psi^{(1)}_{n,0}(\gamma)$. This means the wave function component $\psi^{(1)}_{n,0}(\gamma)$ must be real. From the particle-current formula [see Eq. (28)], we obtain the immediate result $I^{\rm G}_{n,0;n+1,0} = 0$, the very revelation of the zero particle current in the row $m = 0$. If the time-reversal symmetry is conserved ($\gamma = 0, \pm\pi$), the matrix form of $H_{\rm I}$ is real and symmetrical, and then all the eigenstates of $H_{\rm I}$ must be real vectors, e.g., $\psi^{(1)*}_{n,0}(\gamma) \equiv \psi^{(1)}_{n,0}(\gamma)$. This also implies zero particle current along the central row. In contrast to the two-leg ladder [40, 57], the double (or three-leg) ladder is the minimal configuration for which chiral currents at the edges can be sharply distinguished from the behavior of the bulk [55].

C. Vortex number

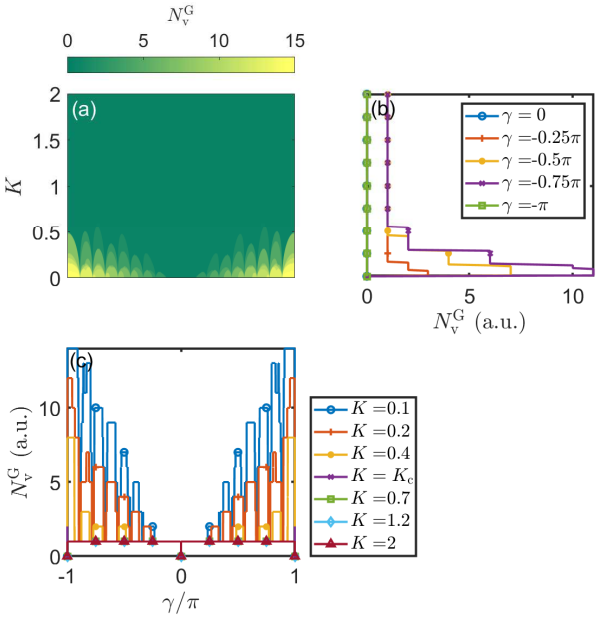

FIG. 4. (color online) Vortex number $N_{\rm v}$ plotted (a) against the effective magnetic flux γ and coupling ratio K, (b) against K for different γ, and (c) against γ for different K. In (b), the curve for $\gamma = 0$ is covered by that for $\gamma = \pi$, while in (c), the curves for $K = 0.7$ and 1.2 are covered by that for $K = 2$. Here, $K_c = 0.55$. The lattice width (length) is $W = 3$ ($L = 17$).

Here, we will introduce the finite-size effect that is not reported in the two-leg ladder [40, 57]. In Sec. III A, we have demonstrated there is always one minimum point on the energy bands, corresponding to the unique single-particle ground state $b^{\dagger}_{k_x=0}|0\rangle$ [see Eq. (21)], where $|0\rangle$ is the global ground state. If the ladder length L approaches infinity, we can approximately think the single-particle ground state in the open-boundary condition is $|G\rangle = b^{\dagger}_{k_x=0}|0\rangle$, whose wave function is therefore $\psi^{(1)}_{nm} = e^{i\gamma mn} e_m(0)/\sqrt{L}$. Here, $(e_{-1}(0), e_0(0), e_1(0))^{\intercal}$ is the eigen vector of $h(k_x)|_{k_x=0}$ with the smallest eigen value. Then, the particle current along the column direction can be calculated as

$$\begin{aligned} I^{\rm G}_{n,-1;n,0} &= I^{\rm G}_{n,0;n,1} \equiv I^{\rm G}_n \\ &= -ig_y \psi^{(1)}_{n,0}\left(e^{i\gamma n}\psi^{(1)}_{n,-1} - \text{c.c.}\right) \\ &= 0. \end{aligned} \tag{29}$$

Simultaneously, the particle current along the edge rows are $I^{\rm G}_{n,-1,;n+1,-1} = -I^{\rm G}_{n,1;n+1,1} = -(2g_x/L)\,|e_{-1}(0)|^2 \sin\gamma$. This means there is always one mere big vortex. However, the practical length L can not be infinite. In the below, we will show for a practical finite length L, the vortex number can exhibit rich phenomena according to different effective magnetic flux γ and coupling ratio K.

Now, we investigate how the vortex number changes against the effective magnetic flux γ and coupling ratio K. As shown in Fig. 4(a), the vortex number is symmetric about the axis $\gamma = 0$. In addition, the vortex number exceeding one merely occurs on left and right bottom corners, where one also find some discrepancies with zero vortex numbers. In Fig. 4(b), the vortex number is plotted against K for $\gamma = 0$, -0.25π, -0.5π, -0.75π, and $-\pi$, respectively. It is clearly shown that the vortex number decreases as K becomes larger. Also, there exists a threshold of K for each specified γ, above which, the vortex number will remain one steadily. In Fig. 4(c), the vortex number is plotted against γ for $K = 0.1$, 0.2, 0.4, $K_{\rm c}$, 0.7, 1.2, and 2, respectively. Here, $K_{\rm c}$ is the global threshold of K, above which the vortex number becomes one whatever γ takes. In the present case $N = 17$, $K_{\rm c} = 0.55$ can be numerically obtained. As in Fig. 4(a), we also see in Fig. 4(c) the symmetry about $\gamma = 0$. When $|\gamma|$ approaches zero, we see the vortex number first drops in an oscillating manner and then remains one for γ exceeding a particular threshold. Before this threshold is met, there are pieces of intervals along the γ axis where only one vortex occurs, which however are never reported in the case of two-leg ladder [40, 57]. There also exists the global threshold of γ, above which the vortex number always remains one whatever K takes. In this case of $L = 17$, we can obtain this global threshold is $\gamma_{\rm c} = 0.14\pi$. As previously mentioned, at the time-reversal symmetric points ($\gamma = 0, \pm\pi$), the energy eigenstates are purely real vectors, and thus there is no particle currents according to Eq. (28), which is why we observe zero vortex number at these points in Fig. 4(c).

D. Chiral current

To better quantify the chirality manifested in the vortices, we here introduce the chiral current operator, which, by definition, is namely

$$I_{\rm c} = I_{x1} - I_{x,-1}. \tag{30}$$

Here, $I_{xm} = \sum_n I_{nm;n+1,m}$ represents the sum of all the particle currents along the mth row. The mean chiral current under the single-particle ground state is denoted by $I^{\rm G}_{\rm c} = \langle G|I_{\rm c}|G\rangle$, which is similar to the definition in Eq. (28). Figure 5 has shown how the chiral current is influenced by the

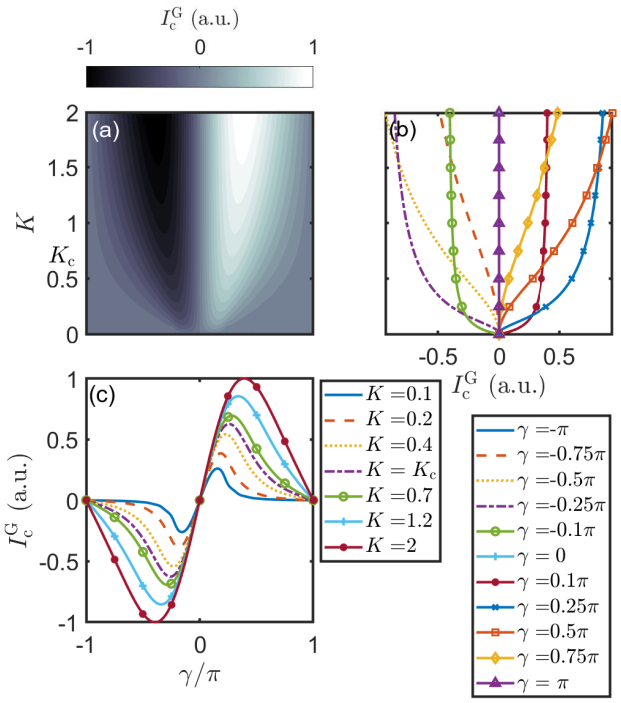

FIG. 5. (color online) Chiral current I_c^G (normalized by its maximum value) plotted (a) against the effective magnetic flux γ and coupling ratio K, (b) against the coupling ratio K for different effective magnetic flux γ, and (c) against the effective magnetic flux γ for different coupling ratio K. Note that in (c), the curves for $\gamma = 0$, and $\gamma = \pm\pi$ coincide.

effective magnetic flux γ and the coupling ratio K, where I_c^G has been normalized by its maximum. In Figs. 5(a)-(c), we see the asymmetry about the axis $\gamma = 0$ of the chiral current, an analogue to the motion of the charged particle governed by the Lorentz force. In Fig. 5(b), we can clearly see that when $|\gamma|$ is increased from 0 to π, the curve of the chiral current against K first leaves from the axis $K = 0$ and then comes back. In Fig. 5(c), one can find that for rising K, the variation of the chiral current against γ resembles the sinusoidal function better and better.

E. Multi-band model

Now, we investigate how the energy bands change when the lattice width W gradually becomes large, where the boundary is considered open (closed) along the m (n) direction. In Fig. 6, the energy bands are plotted for $W = 50$, 10, 5, and 3, respectively, where we have chosen the effective magnetic flux $\gamma = 2\pi/5$, and coupling strengths $g_x = g_y = 2\pi \times 4$ MHz. One can find that when W is small [see Figs. 6(a) and 6(b)], the band number is identical to W, and all bands exhibit edge populations. However, when W becomes large [see Figs. 6(c) and 6(d)], the band number is determined by γ. For example, if $\gamma/2\pi$ is rational, i.e., $\gamma = 2\pi P/Q$ with P and Q coprime integers, the band number is namely the denominator

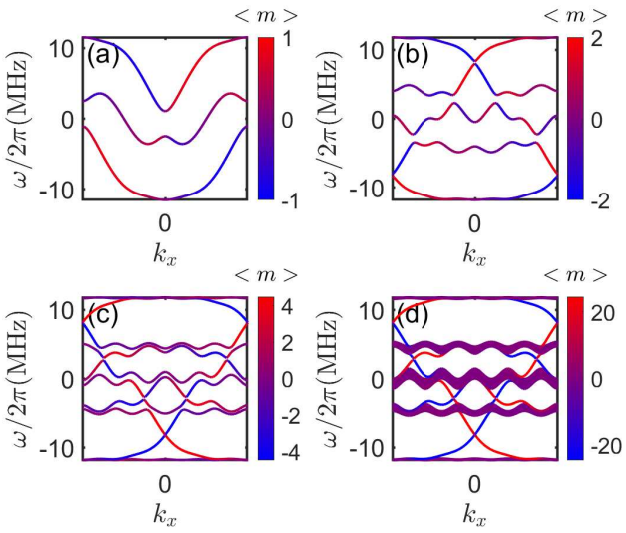

FIG. 6. (color online) Energy bands for the lattice width (a) $W = 3$, (b) $W = 5$, (c) $W = 10$, and (d) $W = 50$. We have chosen the effective magnetic flux $\gamma = \frac{2\pi}{5}$, and coupling strengths $g_x = g_y = 2\pi \times 4$ MHz.

Q. That's why we see five bands in Figs. 6(c) and 6(d), where $\gamma = 2\pi/5$ implies $P = 1$ and $Q = 5$.

The edge state in Fig. 6 is topological phenomenon, which, according to the bulk-edge correspondence [44, 45], can be explained via the Chern number for periodical boundaries. In terms of the jth energy band, the Chern number can be calculated via the formula [53]

$$C_j = \frac{1}{2\pi i}\int \mathrm{d}^2\mathbf{k} F_{xy}^{(j)}(\mathbf{k}), \tag{31}$$

where the integrand is called the Berry curvature and defined by the bulk eigenstate $|u_j(\mathbf{k})\rangle$, i.e., $F_{xy}^{(j)}(\mathbf{k}) = \langle\partial_{k_x}u_j(\mathbf{k})|\partial_{k_y}u_j(\mathbf{k})\rangle - \langle\partial_{k_y}u_j(\mathbf{k})|\partial_{k_x}u_j(\mathbf{k})\rangle$. The Berry curvature reflects the $\mathbf{k}$-dependent adiabatic evolution of the bulk eigenstate. For $\gamma = 2\pi P/Q$, the unit cell possesses a size of $1 \times Q$. Thus, adopting the transformation

$$a_{sQ+r,m} = \frac{1}{\sqrt{WL/Q}}\sum_{\mathbf{k}} e^{ik_y m + isQk_x} S_{r,\mathbf{k}}^{-}, \tag{32}$$

where $k_y \in [0, 2\pi]$ and $k_x \in [0, 2\pi/Q]$, the lattice-space Hamiltonian in Eq. (20) can be transformed into $H = \sum_{\mathbf{k}} S_{r,\mathbf{k}}^{+} h(\mathbf{k}) S_{r,\mathbf{k}}^{-}$, where $S_{\mathbf{k}}^{-} = \left(S_{0,\mathbf{k}}^{-}, \cdots, S_{Q-1,\mathbf{k}}^{-}\right)^{\intercal}$, $S_{r,\mathbf{k}}^{+} = \left(S_{\mathbf{k}}^{-}\right)^{\dagger}$ and the matrix element of the single-particle Hamiltonian $h(\mathbf{k})$ holds the form

$$\begin{aligned} h_{pq}(\mathbf{k}) = &-\hbar g_x\left(\delta_{p,q+1} + \delta_{p,q-1}\right) \\ &-\hbar g_x\left[e^{ik_xQ}\delta_{p,q-(Q-1)} + e^{-ik_xQ}\delta_{p,q+(Q-1)}\right] \\ &+2\hbar g_y\cos\left(k_y - \gamma q\right)\delta_{p,q}. \end{aligned} \tag{33}$$

Then, via numerically diagonalizing the single-particle Hamiltonian $h(\mathbf{k})$, the bulk eigenstate $\left|u^{(j)}(\mathbf{k})\right\rangle$, Berry curvature $F_{xy}^{(j)}(\mathbf{k})$, and even the Chern number can be successively obtained.

In Fig. 7, we have focused on the special case $g_x = g_y = 2\pi \times 4\,\mathrm{MHz}$, where the energy bands and the Berry curvature for each band have been plotted. The peaks or dips of the Berry curvature of mainly occur where the bands approaches each other (see Appendix. D). After integrating the Berry curvatures, the Chern numbers can be obtained as $C_1 = C_2 = C_4 = C_5 = -1$ and $C_3 = 4$. The winding numbers for the edge states in the jth gap can be further calculated by the formula $I_j = \sum_{j' \leq j} C_{j'}$, finally yielding $I_1 = -1$, $I_2 = -2$, $I_3 = 2$, $I_4 = 1$, and $I_5 = 0$, which agrees with how the edge states merge and escape the bulk in Figs. 6(c) and 6(d).

IV. HOFSTADTER BUTTERFLY

The Harper Hamiltonian engineered can exhibit the Hofstadter-butterfly structure [54] if we present the energy levels changing as the effective magnetic flux γ. In Fig. 8, we have focused on a concrete case, where the lattice width $W = 3$, lattice length $L = 17$, and coupling strengths $g_x = g_y = 2\pi \times 4\,\mathrm{MHz}$. In Fig. 8(a), we have chosen the n-open and m-closed boundary condition, which reproduce the original Hofstadter problem [54]. However, the closed boundary condition is difficult to implement using the current planar fabrication technology. Thus, in Fig. 8(b), the n-open and m-open boundary condition is investigated for comparison. We find the energy levels still constitute a butterfly structure. However, the random dots in Fig. 8(b) become regular in Fig. 8(a). We think this can be fundamentally attributed to the m-open boundary condition.

V. EXPERIMENTAL DETAILS

A. Generating the single-particle ground state

To observe the chiral current patterns in the double ladder, one prerequisite is to generate the single-particle ground state $|G\rangle$. In the realistic experiment, the initial state is normally the vacuum state $|0\rangle$ after sufficient cooling in the dilution refrigerator. Thus, we need to generate the single-particle ground sate from the vacuum state. Here, we continue to adopt the state-generation method employed in our previous paper on the two-leg ladder model [40]. In detail, we assume all the transmons are classically driven, which appears as an additional term

$$H_{\mathrm{g}} = \hbar \sum_{n=-N}^{N-1} \sum_{m=-M}^{M-1} \Omega_{nm} e^{-i\nu_m t} a_{nm}^{\dagger} + \mathrm{H.c.}. \tag{34}$$

in the original picture. Here, we assume the driving frequencies take $\nu_m = \omega_{\mathrm{o}} + \nu$ ($\nu_m = \omega_{\mathrm{e}} + \nu$) for m odd (even). Thus, in the interaction picture, the driving Hamiltonian H_{g} becomes

$$\begin{aligned} H_{\mathrm{g,I}} &= \hbar \sum_{n=-N}^{N-1} \sum_{m=-M}^{M-1} \Omega_{nm} e^{-i\nu t} a_{nm}^{\dagger} + \mathrm{H.c.} \\ &= \hbar \sum_{j=1}^{LW} \Omega_j' e^{-i\nu t} S_j^{\dagger} + \mathrm{H.c.}, \end{aligned} \tag{35}$$

where $\Omega_j' = \sum_{n=-N}^{N-1} \sum_{m=-M}^{M-1} \Omega_{nm} \psi_{nm}^{(j)*}$ represents the driving strength that stimulates the single-particle state $|E_j\rangle$. Next, the complex driving strength Ω_{nm} is specified as $\Omega_{nm} = \psi_{nm}^{(1)} \Omega$, which further transforms $H_{\mathrm{g,I}}$ into $H_{\mathrm{g,I}} = \hbar\Omega S_1^{\dagger} e^{-i\nu t} + \mathrm{H.c.}$.The detuning is further assumed to take $\nu = E_1/\hbar$, and then there is an Rabi oscillation between the vacuum sate $|0\rangle$ and single-particle state $|E_1\rangle$. If a $\frac{\pi}{2}$ pulse is applied (i.e., $\Omega t = \frac{\pi}{2}$), the single-particle ground state $|G\rangle = |E_1\rangle$ can be obtained in just one step from the vacuum state $|0\rangle$. Suppose the relaxation and dephasing rates are γ_{nm} and Γ_{nm} for the transmon at the site nm, the equivalent relaxation and dephasing rates between the states $|G\rangle$ and $|0\rangle$ are $\gamma_1 = \sum_{n=-N}^{N} \sum_{m=-M}^{M} \left|\psi_{nm}^{(1)}\right|^2 \gamma_{nm}$ and $\Gamma_1 = \sum_{n=-N}^{N} \sum_{m=-M}^{M} \left|\psi_{nm}^{(1)}\right|^2 \Gamma_{nm}$. Then using the Lindblad master equation, the generation fidelity of the single-particle ground state can be calculated as $\langle G| \hat{\rho} |G\rangle = \frac{1}{2}\left[1 - e^{-\frac{1}{2}(\gamma_1 + \frac{\Gamma_1}{2})t} \cos(2\Omega t)\right]$. One can see that in the strong-driving regime $\Omega \gg \gamma_1, \Gamma_1$, the effects of the dissipation can in principle be neglected for a $\frac{\pi}{2}$ pulse.

B. Measuring the particle current

Here, we discuss the scheme on measuring the particle current, an indispensable step towards depicting the current pattern and then counting the vortex number. The measurement procedure also follows our previous work [40]. For example, to measure the particle current between two adjacent sites nm and $n'm'$ ($n'm' = n+1, m$, or $n, m+1$), we first decouple any other site that connects to nm or $n'm'$ and then investigate the Rabi oscillation between nm and $n'm'$. Then, in the strong-coupling regime, $|g_x|, |g_y| \gg \gamma_{nm}, \Gamma_{nm}$, the time-dependent population difference between nm and $n'm'$ can be represented as

$$P_{nm;x}(t) = e^{-i\gamma_{nm;x} t} \left[\cos(2g_x t) + \sin(2g_x t) \frac{I_{nm;x}^{\mathrm{G}}}{g_x}\right] \tag{36}$$

for the site index $n'm' = n+1, m$, where the decay factor $\gamma_{nm;x} = (\gamma_{nm} + \gamma_{n+1,m} + \Gamma_{nm} + \Gamma_{n+1,m})/4$, or similarly,

$$P_{nm;y}(t) = e^{-i\gamma_{nm;y} t} \left[\cos(2g_y t) + \sin(2g_y t) \frac{I_{nm;y}^{\mathrm{G}}}{g_y}\right] \tag{37}$$

for the site index $n'm' = n, m+1$, where the decay factor $\gamma_{nm;y} = (\gamma_{nm} + \gamma_{n,m+1} + \Gamma_{nm} + \Gamma_{n,m+1})/4$. Via fitting the experimental data of the population difference with Eqs. (36) and (37), the particle current between the sites nm and $n'm'$ can in principle be extracted.

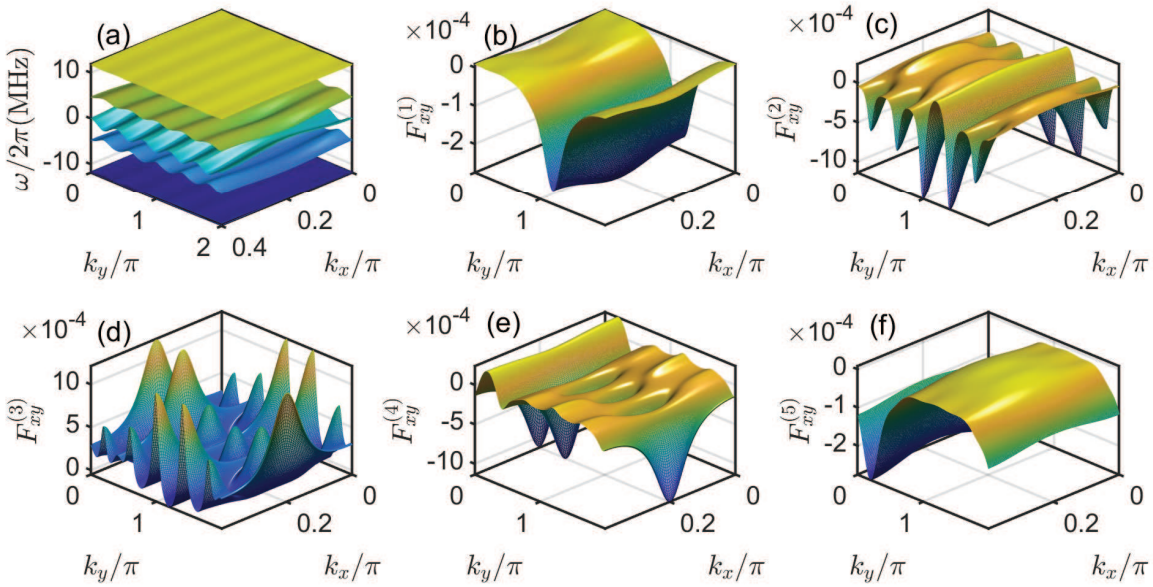

FIG. 7. (color online) (a) Energy bands and Berry curvatures for the (b) first, (c) second, (d) third, (e) fourth and (f) fifth energy band. Here, we have taken the coupling strengths $g_x = g_y = 2\pi \times 4$ MHz and the effective magnetic flux $\gamma = 2\pi/5$. The Chern numbers are respectively $C_1 = C_2 = C_4 = C_5 = -1$ and $C_3 = 4$.

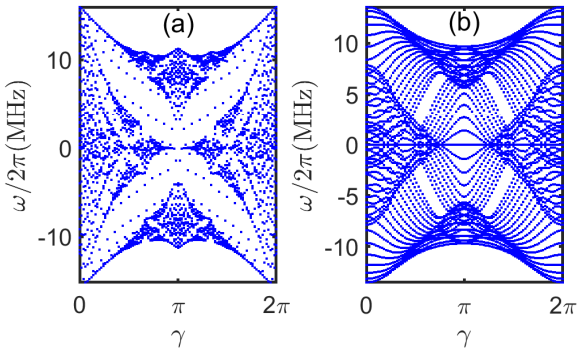

FIG. 8. Energy for γ changing from 0 to 2π, with $W = 3$, $L = 17$, $g_x = g_y = 2\pi \times 4$ MHz. In (a), the boundaries are open (periodical) in the x (y) direction, while in (b), the boundaries are open in both directions.

C. Measuring the Hofstadter-butterfly spectrum

The Hofstadter-butterfly spectrum can be measured using a similar method adopted in the one-dimensional Harper model [35]. From the global ground state $|0\rangle = \prod_{nm} |0\rangle_{nm}$, first we only prepare the nmth transmon to $(|0\rangle_{nm} + |1\rangle_{nm})/\sqrt{2}$, where $|1\rangle_{nm} = \sigma_{nm}^{+} |0\rangle_{nm}$ and $\sigma_{nm}^{+} = |1\rangle_{nm} \langle 0|_{nm}$ denotes the single-qubit raising operator. Here, note that in the single-particle regime, σ_{nm}^{+} (σ_{nm}^{-}) is equivalent to the bosonic creation (annihilation) operator $a_{nm}^{\dagger}$ (a_{nm}). Then, the product state of all the qubits takes $(|0\rangle + |1_{nm}\rangle)/\sqrt{2}$ with $|1_{nm}\rangle = \sigma_{nm}^{+} |0\rangle$. Then, we synthesize the specific two-dimensional Harper Hamiltonian [see Eq. (20)] and record the evolution of the raising operator, termed by $\chi_{nm}(t) = 2\langle \sigma_{nm}^{+}(t) \rangle$. Technically, the quantity $\chi_{nm}(t)$ amounts to measurements of the Pauli X operator σ_{nm}^{x} and Pauli Y operator σ_{nm}^{y} considering $\sigma_{nm}^{+} = (\sigma_{nm}^{x} + i\sigma_{nm}^{y})/2$, finally leading to $\chi_{nm}(t) = \langle \sigma_{nm}^{x}(t) \rangle + i \langle \sigma_{nm}^{y}(t) \rangle$. When we vary nm to cover all the sites, the initial states construct a complete basis and thus each energy eigenstate will have some overlap with at least one initial state, which guarantees that the energy spectrum is fully resolved. Thus, we will average $\chi_{nm}(t)$ over all the sites and obtain $\bar{\chi}(t) = \frac{1}{LW} \sum_{n=-N}^{N} \sum_{m=-M}^{M} \chi_{nm}(t)$. The strict analysis in Appendix. E presents that the frequencies that occur in the Fourier transform of $\chi(t)$, with a homogeneous amplitude $\frac{1}{LW}$, are the eigenenergies of the Harper Hamiltonian.

D. Measuring the energy bands: a special method

We now discuss how to measure the energy bands in Fig. 6. The detailed method is based on making Fourier transforms of single-particle energy eigenstates in the open-boundary conditions of both directions. We still denote the single-particle energy eigenstate by $|E_j\rangle = \sum_{nm} \psi_{nm}^{(j)} |1_{nm}\rangle = \sum_{nm} \psi_{nm}^{(j)} \sigma_{nm}^{\dagger} |0\rangle$ for the eigen energy E_j (see Sec. III B).

First, we should synthesize the single-particle state $|E_j\rangle$. The method is identical to the generation of single-particle ground state (see Sec. V A) except that $\psi_{nm}^{(1)}$ is replaced with $\psi_{nm}^{(j)}$ (e.g., $\Omega_{nm} = \psi_{nm}^{(j)} \Omega$).

Then, we investigate how to measure the state $|E_j\rangle$, or rather, $\psi_{nm}^{(j)}$. Although the actual state could vary due to experimental errors, we still use the same symbols here for convenience. The direct measurement of all the transmons will

provide $\left|\psi_{nm}^{(j)}\right|^2$ or equivalently, $\left|\psi_{nm}^{(j)}\right|$.

What remains to be determined is the phase of $\psi_{nm}^{(j)}$, which we denote by $\theta_{nm}^{(j)}$. To do this, the strategy is to measure the relative phase between adjacent sites, e.g., $\theta_{nm}^{(j)}-\theta_{n'm'}^{(j)}$ between the sites nm and $n'm'$ ($n'm'=n+1,m$ or $n'm'=n,m+1$). This pair of sites is immediately decoupled from the other sites once $|E_j\rangle$ is generated. Meanwhile, the intersite coupling strength $g_{nm;n'm'}$ is tuned appropriately for a time t_1 to generate what we call a X-$\frac{\pi}{4}$ pulse ($g_{nm;n'm'}t_1=\frac{\pi}{4}$), which gives the final state $\psi_{nm}^{(j)}(t_1)=\left[\psi_{nm}^{(j)}-i\psi_{n'm'}^{(j)}\right]/\sqrt{2}$ and $\psi_{n'm'}^{(j)}(t_1)=\left[\psi_{n'm'}^{(j)}-i\psi_{nm}^{(j)}\right]/\sqrt{2}$. Now, the measurement of the qubits at both sites provides the experimental data of $\left|\psi_{nm}^{(j)}(t_1)\right|^2$ and $\left|\psi_{n'm'}^{(j)}(t_1)\right|^2$, either of which will offer the same information of the relative phase between both sites. For example, the datum of $\left|\psi_{nm}^{(j)}(t_1)\right|^2$ gives the relation

$$\left|\psi_{nm}^{(j)}(t_1)\right|^2=\frac{1}{2}\left|\psi_{nm}^{(j)}\right|^2+\frac{1}{2}\left|\psi_{n'm'}^{(j)}\right|^2+\left|\psi_{nm}^{(j)}\right|\left|\psi_{n'm'}^{(j)}\right|\sin\left[\theta_{n'm'}^{(j)}-\theta_{nm}^{(j)}\right]. \quad (38)$$

This implies $\sin\left[\theta_{nm}^{(j)}-\theta_{n'm'}^{(j)}\right]$ can be extracted as $\left|\psi_{nm}^{(j)}\right|$ and $\left|\psi_{n'm'}^{(j)}\right|$ have been known. However, to uniquely determine $\theta_{nm}^{(j)}-\theta_{n'm'}^{(j)}$, we still need the information of $\cos\left[\theta_{nm}^{(j)}-\theta_{n'm'}^{(j)}\right]$. This can be performed via inserting a free rotation of both qubits before applying the X-$\frac{\pi}{4}$ pulse. To realize this, we switch off the coupling between both sites and detune the qubit frequency ω_{nm} ($\omega_{n'm'}$) with $\frac{\Delta_{nm}}{2}$ ($-\frac{\Delta_{nm}}{2}$). After a time t_0, we generate what we call a Z-$\frac{\pi}{2}$ pulse ($\Delta_{nm}t_0=\frac{\pi}{2}$). Then, the state components $\psi_{nm}^{(j)}$ and $\psi_{n'm'}^{(j)}$ evolve to $\psi_{nm}^{(j)}(t_0)=e^{\frac{-i\pi}{4}}\psi_{nm}^{(j)}$ and $\psi_{nm}^{(j)}(t_0)=e^{\frac{i\pi}{4}}\psi_{nm}^{(j)}$. Next, we apply the X-$\frac{\pi}{4}$ pulse (($g_{nm;n'm'}t_1=\frac{\pi}{4}$)) and the state components further evolve to $\psi_{nm}^{(j)}(t_1+t_0)=\left[\psi_{nm}^{(j)}(t_0)-i\psi_{n'm'}^{(j)}(t_0)\right]/\sqrt{2}$ and $\psi_{n'm'}^{(j)}(t_1+t_0)=\left[\psi_{n'm'}^{(j)}(t_0)-i\psi_{nm}^{(j)}(t_0)\right]/\sqrt{2}$. Afterwards, the readout of both qubits is implemented, and thus both $\left|\psi_{nm}^{(j)}(t_1+t_0)\right|^2$ and $\left|\psi_{n'm'}^{(j)}(t_1)\right|^2$ are accessible quantities. The measurement of the nmth qubit gives the relation

$$\left|\psi_{nm}^{(j)}(t_1+t_0)\right|^2=\frac{1}{2}\left|\psi_{nm}^{(j)}\right|^2+\frac{1}{2}\left|\psi_{n'm'}^{(j)}\right|^2+\left|\psi_{nm}^{(j)}\right|\left|\psi_{n'm'}^{(j)}\right|\cos\left[\theta_{n'm'}^{(j)}-\theta_{nm}^{(j)}\right] \quad (39)$$

From Eqs. (38) and (39), the relative phase $\theta_{n'm'}^{(j)}-\theta_{nm}^{(j)}$ can be uniquely determined if it is confined to the regime $(-\pi,\pi]$. Now, the measurement of the relative phase between to adjacent sites is completed. To determine the phases of all wave function components, we should measure all the relative phases between the sites nm and $n+1,m$ for $-N\leq n\leq N-1$ and $-M\leq m\leq M$, and those between $-N,m$ and $-N,m+1$ for $-M\leq m\leq M-1$. Supposing $\psi_{-N,-M}\geq 0$, then the phase of $\psi_{nm}^{(j)}$ can be represented as $\theta_{nm}^{(j)}=\sum_{p=-M+1}^{m}\left[\theta_{-N,p}^{(j)}-\theta_{-N,p-1}^{(j)}\right]+\sum_{p=-N+1}^{n}\left[\theta_{p,m}^{(j)}-\theta_{p-1,m}^{(j)}\right]$.

The last step for constructing the energy bands is to make space Fourier transformation of $\psi_{nm}^{(j)}$. The single-particle state $\psi_{nm}^{(j)}$ must be the superposition of the states with the same energy in Fig. 6, that is,

$$|E_j\rangle=\sum_{n=-N}^{N}\sum_{m=-M}^{M}\psi_{nm}^{(j)}a_{nm}^{\dagger}|0\rangle=\sum_{\hbar\omega(k_x)=E_j}\psi_{k_xm}b_{k_x,m}^{\dagger}|0\rangle. \quad (40)$$

From Eq. (21), which establishes the relation between a_{nm} and $b_{k_x,m}$, we can further obtain the Fourier expansion of $\psi_{nm}^{(j)}$, which is

$$\psi_{nm}^{(j)}=\sum_{\hbar\omega(k_x)=E_j}\frac{\psi_{k_xm}}{\sqrt{L}}e^{i(\gamma m+k_x)n}. \quad (41)$$

To quantify the quasimomentum distribution of $\psi_{nm}^{(j)}$, we calculate the Fourier transformation of $\psi_{nm}^{(j)}$ and seek their square sum over m, thus leading to the quantity

$$\Pi_j(k_x)=\sum_{m=-M}^{M}\left|\sum_{n=-N}^{N}\frac{e^{-i(\gamma mn+k_xn)}}{\sqrt{L}}\psi_{nm}^{(j)}\right|^2=\sum_{m=-M}^{M}\left|\sum_{\hbar\omega(k_x')=E_j}\frac{\psi_{k_x'm}}{L}\frac{\sin\frac{(k_x-k_x')L}{2}}{\sin\frac{k_x-k_x'}{2}}\right|^2. \quad (42)$$

Via seeking the peak value of $\Pi_j(k_x)$, we obtain the point $(k_x',\omega(k_x'))$ where $\hbar\omega(k_x')=E_j$. When we plot all the points $(k_x',\omega(k_x'))$, the energy bands can in principle be restored. In Fig. 9, the measured energy bands are shown by the colored dots. One can see that they agree very well with the strict results indicated by the solid grey curves (see Fig. 6). Via observing how the edge states emerge into and escape from the bulk states, we can then obtain the winding number and also the Chern number [44, 45].

However, the method introduced here needs many details of the Hamiltonian. For example, when generating the energy eigenstate $|E_j\rangle$, we need its wave function $\psi_{nm}^{(j)}$, which is fundamentally determined by the concrete Hamiltonian parameters. The contradiction lies in that if we know all the details of the Hamiltonian, we can straightforwardly calculate the energy bands. The significance of measuring the energy eigenstate $|E_j\rangle$ and also ω-k_x dependence using this method is mostly exhibited in testing whether the experimental results agree with the theoretical ones. Thus, in the next subsection Sec. V E, we will develop a method of measuring energy bands without knowing all the details of the Hamiltonian. But the latter does pose a way more severe requirement on the decoherence time if the qubit number is very large.

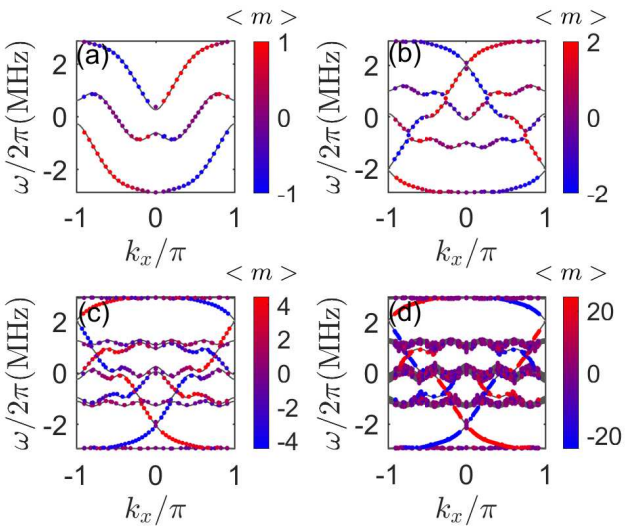

FIG. 9. (color online) Measured energy bands (colored dots) for the lattice width (a) $W = 3$, (b) $W = 5$, (c) $W = 10$, and (d) $W = 50$. We have chosen the effective magnetic flux $\gamma = \frac{2\pi}{5}$, and coupling strengths $g_x = g_y = 2\pi \times 4\,\mathrm{MHz}$. The grey solid curves are strict energy bands (see Fig. 6) for comparison.

E. Measuring the energy bands: a general method

Here, we introduce a more general method to measure the energy bands. Supposing we initially excite the global ground state $|0\rangle$ to the single-particle state

$$|\psi_{nm}(0)\rangle = |nm\rangle = a_{nm}^{\dagger}|0\rangle = \sum_{j=1}^{LW} \psi_{nm}^{(j)*} |E_j\rangle , \tag{43}$$

then we engineer the Harper Hamiltonian H_{I} (see Eq. 20). After a time t, the system will freely evolve to

$$|\psi_{nm}(t)\rangle = \sum_{j=1}^{LW} \psi_{nm}^{(j)*} e^{-i\omega_j t} |E_j\rangle \tag{44}$$

with $\omega_j = E_j/\hbar$. Here, the wave function $|\psi_{nm}(t)\rangle$ can be measured using a similar method mentioned in Sec. V D.

To find all the eigen frequencies ω_j, we first perform the time-domain Fourier transformation of $|\psi(t)\rangle$, giving

$$\begin{aligned} \left|\tilde{\psi}_{nm}(\omega)\right\rangle &= \frac{1}{T}\int_0^T e^{i\omega t} |\psi_{nm}(t)\rangle \,\mathrm{d}t \\ &= \sum_j \psi_{nm}^{(j)*} e^{i\frac{(\omega-\omega_j)T}{2}} \left[\frac{\sin\frac{(\omega-\omega_j)T}{2}}{\frac{(\omega-\omega_j)T}{2}}\right] |E_j\rangle . \end{aligned} \tag{45}$$

Please note that $\left|\tilde{\psi}_{nm}(\omega)\right\rangle$ is not necessarily normalized. Next, we define what we call the feature function

$$\begin{aligned} F(\omega) &= \sum_{nm} \left\langle \tilde{\psi}_{nm}(\omega) \middle| \tilde{\psi}_{nm}(\omega) \right\rangle \\ &= \sum_j \frac{\sin^2\frac{(\omega-\omega_j)T}{2}}{\left[\frac{(\omega-\omega_j)T}{2}\right]^2}. \end{aligned} \tag{46}$$

Hereafter, we suppose the system can coherently evolve for a sufficiently long time, i.e., $T|\omega_j - \omega_{j-1}| \gg 1$, where T should not exceed the system decoherence time T_{coh}. Via seeking the peaks of $F(\omega)$, we can find all the eigen frequencies $\{\omega_j\}_{j=1}^{LW}$. This method can also be applied to the measurement of Hofstadter-butterfly spectrum (see Appendix. E).

The energy eigenstate $|E_j\rangle$ can be restored from the measured data $\left|\tilde{\psi}_{nm}(\omega)\right\rangle$. From Eq. (45), we find that $\left|\tilde{\psi}_{nm}(\omega_j)\right\rangle \approx \psi_{nm}^{(j)*}|E_j\rangle$, having assumed $T|\omega_j - \omega_{j-1}| \gg 1$. To remove the ambiguity of the phase factor of $|E_j\rangle$, we implicitly think $\arg\left\{\psi_{n_j m_j}^{(j)}\right\} = 0$, which further means $\arg\left\{\psi_{nm}^{(j)}\right\} = -\arg\left\{\langle n_j m_j \left|\tilde{\psi}_{nm}(\omega_j)\right\rangle\right\}$. Then, we are convinced to define the fictitious energy eigenstate $\left|\tilde{E}_j\right\rangle$, i.e.,

$$\left|\tilde{E}_j\right\rangle = \sum_{nm} \tilde{M}(\omega_j)\, e^{-i\arg\left\{\langle n_j m_j | \tilde{\psi}_{nm}(\omega_j)\rangle\right\}} \left|\tilde{\psi}_{nm}(\omega_j)\right\rangle \tag{47}$$

where $\tilde{M}(\omega_j) = \sqrt{\left\langle \tilde{\psi}_{nm}(\omega_j) \middle| \tilde{\psi}_{nm}(\omega_j)\right\rangle}$ is the norm of $\left|\tilde{\psi}_{nm}(\omega_j)\right\rangle$. One can easily prove that in the limit $T|\omega_j - \omega_{j-1}| \gg 1$, $\tilde{M}(\omega_j) \approx \left|\psi_{nm}^{(j)}\right|$ and $\left|\tilde{E}_j\right\rangle \approx \sum_{nm}\left|\psi_{nm}^{(j)}\right|^2 |E_j\rangle = |E_j\rangle$.

Having obtained the energy eigenstate $|E_j\rangle$ (or rather, $\psi_{nm}^{(j)}$), we also define the quantity $\Pi_j(k_x)$ as in Eq. (42). Through finding the peaks of $\Pi_j(k_x)$, we can establish the dependence between the ω and k_x' with $\hbar\omega(k_x') = E_j$.

In fact, after the eigenstates and the eigen energies, the Hamiltonian can be constructed as

$$\tilde{H} = \sum_j E_j \left|\tilde{E}_j\right\rangle \left\langle \tilde{E}_j\right| . \tag{48}$$

This means that our method offers a way to construct the Hamiltonian of an unknown system. After the Hamiltonian is reconstructed, or rather in the tight-binding form, we can also thoroughly analyze the energy bands of the system.

VI. CONCLUSIONS

We have proposed to engineer an ideal system of the single-particle Harper Hamiltonian in a two-dimensional architecture based on interacting transmons mediated by inductive couplers. Through designing a gradiometer form of the mutual

inductance between the coupler and the transmon, the decoherent effect of the environment noise is believed to be mitigated in some extent. Based on this architecture, the chiral or topological phenomena induced by effective magnetic flux are exhaustively studied for the single-particle states according to the explicit size of the Harper model.

First, we have concentrated on the double-ladder (i.e., three-leg ladder) model, which is known as the simplest true-two-dimensional configuration. In contrast to the quasi-two-dimensional two-leg ladder, the double-ladder possesses a central row, thus presenting the concept of bulk. We find the particle current along the central row is always zero, which is fundamentally due to the equivalence between the space symmetry and the time-reversal symmetry. Besides, the interplay between the effective magnetic flux and the coupling ratio (i.e., the ratio between the column and row coupling strengths) results in the vortex-Meissner phase transition. For the given coupling ratio, there exists the critical effective magnetic flux, below which, the Meissner phase is maintained. However, if the critical value is exceeded by the magnitude of the effective magnetic flux, there are staggered transitions between the vortex and Meissner phases, a quite different phenomenon from the case in the two-leg ladder where only the vortex phase exists after the critical effective magnetic flux. In the Meissner phase, the particle currents only populates on the edges, which can thus be treated as the analogue to the quantum Hall effect. The chiral current, defined by the mean particle current between the top and bottom row resembles the squeezed sinusoidal function of the effective magnetic flux. When the coupling ratio becomes larger, the squeezing effect is alleviated and the trend of the curve approaches the sinusoidal function better.

Besides, we have continued to study the multiple-row case of the Harper model. In detail, we increase the row number beyond three and find the energy spectrum in the periodical condition gradually approach the topological energy band. The winding number of the edge states are consistent with the Chern number of the bulk states. We have estimated the lattice size that can exhibit the topological energy band. If we only apply the open-boundary condition to the row direction, the typical Hofstadter-butterfly spectrum will occur. If we apply the open-boundary condition to both the row and column directions, the Hofstadter-butterfly spectrum becomes smoother. The Hofstadter-butterfly spectrum can be measured via investigating the evolution of the single-qubit raising operator.

We have presented two methods on how to measure the topological band structure in two-dimensional superconducting qubit circuits. The first one is based on the excitation and measurement of the single-particle eigen states, which needs the details of the Hamiltonian but requires a loose decoherence time only if it is enough to accomplish the single-particle state generation. In contrast, the second one is based on subsequently excitation of all the qubits and instant measurement of the states during the coherent evolution of a long enough period, which thus should be guaranteed by a decoherence time long enough to discern the discrete energy levels. Both methods need the space-domain Fourier transformation of the wave functions, while, the second one also needs the Fourier transformation of the wavefunction in the time domain. Different from the method in Ref. [35], which mainly focuses on measuring the eigenenergies, our methods have also systematically discussed how to measure and analyze the energy eigenstates. The methods proposed here can be generalized to versatile quantum simulation experiments and are promising for Hamiltonian reconstruction of an unknown system.

VII. ACKNOWLEDGMENTS

Y.J.Z. is supported by Beijing Natural Science Foundation (BNSF) under grants No. 4222064, National Natural Science Foundation of China (NSFC) under the grant No. 11904013, and State Scholarship Fund.

Appendix A: Tunable linear inductive network

Here, we will show that the coupler and surrounding circuit [see Fig. 10(a)] can be equivalent to a simple tunable linear inductive network. In detail, we focus on the interaction is between a pair of adjacent qubits at the site nm and $n'm'$.

First, we assume zero SQUID branch currents at both sites, that is, $I_{nm} = I_{n'm'} = 0$. Then, if we assume the flux drop across the coupler junction is $\Phi^{\mathrm{T}}_{nm;n'm'}$, the should be

$$\Phi^{\mathrm{T}}_{nm;n'm'} + 2L_0 I_{nm;n'm'} - \Phi_{nm;n'm'} = 0 \tag{A1}$$

due to trapped magnetic flux in the coupler loop, where $I_{nm;n'm'} = I_{\mathrm{c}} \sin\left(\frac{2\pi\Phi^{\mathrm{T}}_{nm;n'm'}}{\Phi_0}\right)$ is the coupler junction current, I_{c} the junction critical current, Φ_0 the magnetic flux quantum, and L_0 the self inductance of half the coupler loop. Compared to the junction inductance, which is $L_{\mathrm{T}} = \frac{\Phi_0}{2\pi I_{\mathrm{c}}}$, L_0 is usually negligible. Thus, we disregard the term $2L_0 I_{nm;n'm'}$ in Eq. (A1), yielding $\Phi^{\mathrm{T}}_{nm;n'm'} \approx \Phi_{nm;n'm'}$.

Now we consider nonzero SQUID branch currents I_{nm} and $I_{n'm'}$, which are treated as quantum perturbations to the working point established by Eq. (A1). In this case, the coupler junction is equivalent to a tunable linear inductor [62] in the quantum regime, with the inductance

$$L_{nm;n'm'} = \frac{\Phi_0}{2\pi I_{\mathrm{c}} \cos\left(\frac{2\pi\Phi^{\mathrm{T}}_{nm;n'm'}}{\Phi_0}\right)} \approx \frac{L_{\mathrm{T}}}{\cos\left(\frac{2\pi\Phi_{nm;n'm'}}{\Phi_0}\right)}. \tag{A2}$$

Thus, the circuit in Fig. 10(a) can be simplified into the one in Fig. 10(b) for the perturbative quantum signals.

Last, applying the principle of linear superposition to Fig. 10(b) where the currents I_{nm} and $I_{n'm'}$ are regarded as sources, we can obtain the node fluxes between the SQUIDs and their respective grounding wire as

$$\Phi^{(g)}_{nm} = L_{nm} I_{nm} + M_{nm;n'm'} I_{n'm'}, \tag{A3}$$

$$\Phi^{(g)}_{n'm'} = M_{n'm';nm} I_{nm} + L_{n'm'} I_{n'm'}. \tag{A4}$$

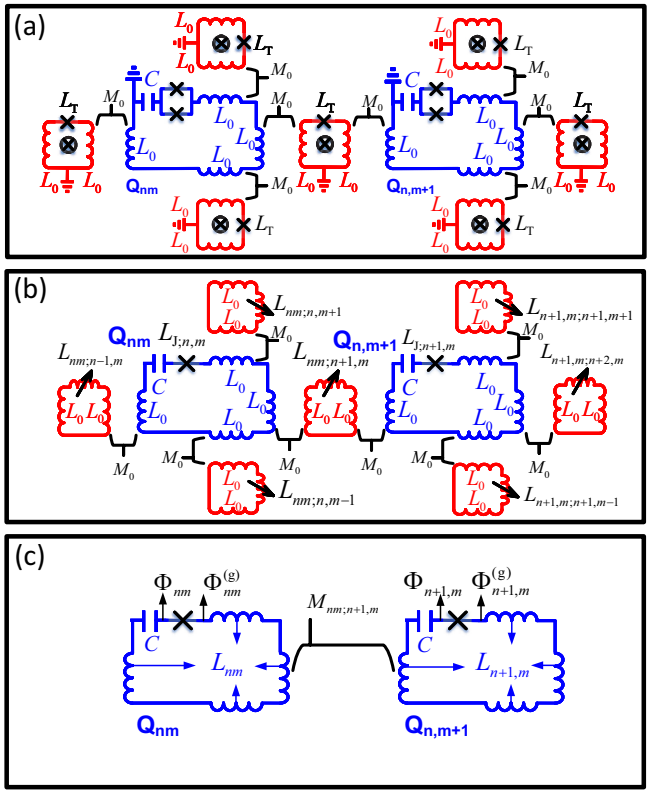

FIG. 10. (a) Coupling circuit diagram between two adjacent qubits Q_{nm} and $\mathrm{Q}_{n+1,m}$. The coupler (colored red) and qubit (colored blue) loop respectively contains two and four segments of self inductance L_0. The coupler junction inductance is L_T and the shunting capacitance of the qubit is C. Besides, the mutual inductance between the qubit and coupler loop is M_0. (b) Simplified coupling circuit diagram with the coupler junction treated as a tunable linear inductance ($L_{nm;n'm'}$ for the coupler between nm and $n'm'$) and the SQUID (superconducting quantum interference device) is replaced by a single junction (with junction inductance $L_{\mathrm{J};nm}$ at nm). (c) The freedom of the coupler has been eliminated. This induces a total self inductance L_{nm} ($L_{n+1,m}$) along the qubit loop at nm ($n+1,m$). The coupler-mediated interaction is modelled by a mutual inductance $M_{nm;n+1,m}$. The node fluxes that construct the Hamiltonian are also indicated (e.g., Φ_{nm}, $\Phi_{nm}^{(\mathrm{g})}$, etc).

Here, L_{pq} and $M_{pq;p'q'}$ indicate the self and mutual inductance, respectively, which can be represented as

$$L_{pq} = 4L_0 + \sum_{p'q'\in\mathbb{C}_{pq}} M_{pq;p'q'}, \tag{A5}$$

$$M_{pq;p'q'} = -\frac{M_0^2}{2L_0 + L_{pq;p'q'}} \tag{A6}$$

$$= -\frac{M_0^2 \cos\left(\frac{2\pi}{\Phi_0}\Phi_{pq;p'q'}\right)}{L_\mathrm{T} + 2L_0\cos\left(\frac{2\pi}{\Phi_0}\Phi_{pq;p'q'}\right)}, \tag{A7}$$

Thus, Fig. 10(b) can be further simplified into the tunable linear inductive network in Fig. 10(c).

Appendix B: Normalized current pattern

Since the vortex number in Fig. 3 is hard to discern, we have plotted the current patterns with all the particle-current amplitudes normalized to one identical value in Fig. 11. As has been shown from the top to bottom row, there are 7, 4, 2, 1 vortices as K takes 0.1, 0.2, 0.4, and 0.7, respectively.

Appendix C: Degeneracy property of the single-particle ground state

Here, we make some remarks about the single-particle ground state (denoted by $\psi_{n,m}^{(1)}$ in the main text) in the case of broken time-reversal symmetry ($0<|\gamma|<\pi$). First, we assume the length of the double-ladder is sufficiently large (say, the length $L\to\infty$). Then, the single-particle ground state in the open-boundary condition must correspond to the ground bulk state. From Fig. 2, we can find that for $0<|\gamma|<\pi$ and not too small g_y/g_x, the minimum energy is achieved at $k_x=0$, where the single-particle ground state must be nondegenerate. For sufficiently small g_y/g_x, we can prove using the perturbative method that the eigen energy at $k_x=0$, which is

$$E_0' \approx -2\hbar g_x - \frac{\hbar g_y^2}{g_x}\frac{1}{1-\cos\gamma}, \tag{C1}$$

is always lower than those at $k_x=\pm\gamma$, which are both

$$E_\gamma' = -2\hbar g_x + \frac{\hbar g_y^2}{2g_x}\frac{1}{1-\cos\gamma}. \tag{C2}$$

Thus, the minimum energy is still achieve at $k_x=0$, implying that the single-particle ground state must be nondegenerate.

However, the have focused on practical ladder length, e.g., $L=17$, which is far from infinity. The single-particle ground state in the open-boundary condition may not the ground bulk state. In this case, we have numerically plotted the frequency interval between the first excited state and the ground state, i.e., $\omega_{21}=\omega_2-\omega_1$, against the practical regimes of γ and K, just as shown in Fig 12. We can conveniently find there is no degeneracy in the regime of interest $0<|\gamma|<\pi$.

In the worst case that the single-particle ground states are degenerate and $\psi_{n,m}^{(1)*}\neq\psi_{n,-m}^{(1)}$, we recombine the ground states as $\psi_{n,m}^{(1,+)}=\psi_{n,-m}^{(1)*}+\psi_{n,m}^{(1)}$ and $\psi_{n,m}^{(1,-)*}=\psi_{n,-m}^{(1)*}-\psi_{n,m}^{(1)}$, where the normalized constants are temporarily ignored. One then finds that $\psi_{n,m}^{(1,+)*}=\psi_{n,-m}^{(1,+)}$ and $\psi_{n,m}^{(1,-)*}=-\psi_{n,-m}^{(1,-)}$, which further induces $\psi_{n,0}^{(1,+)*}=\psi_{n,0}^{(1,+)}$ and $\psi_{n,0}^{(1,-)*}=-\psi_{n,0}^{(1,-)}$. Thus, both $\psi_{n,m}^{(1,+)}$ and $\psi_{n,m}^{(1,-)}$ heralds a zero particle current along the central row [see Eq. (28)].

Appendix D: Calculation of the Chern number

The Chern number for the jth energy band is defined by [60]

$$C_j = \frac{1}{2\pi i}\int \mathrm{d}^2\mathbf{k} F_{xy}^{(j)}(\mathbf{k}), \tag{D1}$$

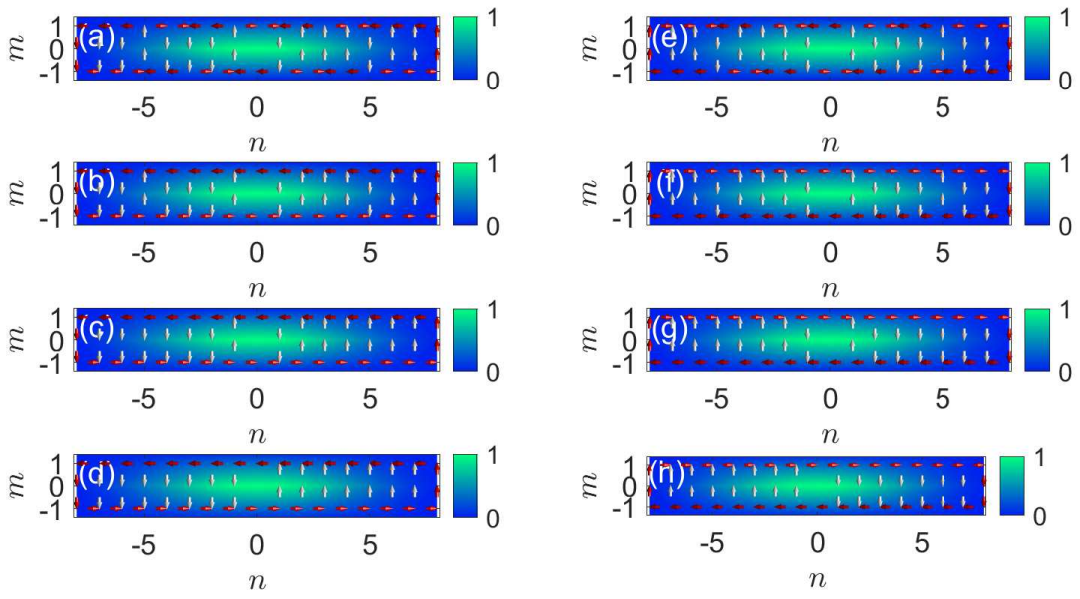

FIG. 11. (color online) Normalized particle current patterns for the effective magnetic flux γ taking (a)-(c) $-\frac{\pi}{2}$ and (d)-(f) $\frac{\pi}{2}$ in a double ladder (lattice width $W = 3$) with the lattice length length $L = 17$. From top to bottom, the coupling strengths along two directions fulfill the conditions $K = 0.1$, 0.2, 0.4, and 0.7, respectively. The particle current between adjacent sites is represented by a arrow whose size implies the current magnitude. We have used the red (green) color for currents along the edge (in the bulk). Beside, the color in the background represents the relative occupation probability in the single-particle ground state.

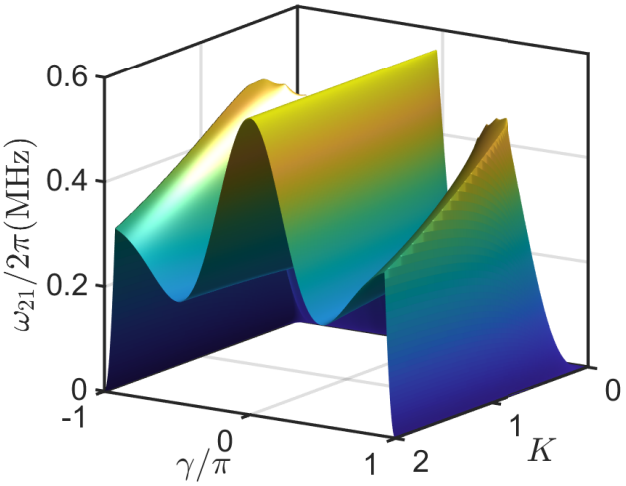

FIG. 12. Frequency interval between the two lowest energy eigenstates $\omega_{21} = \omega_2 - \omega_1$ in the open-boundary condition for the double ladder plotted against the effective magnetic flux γ and coupling ratio K. The lattice width (length) is $W = 3$ ($L = 17$).

where the integrand is the Berry curvature and is of the form

$$F_{xy}^{(j)} = \langle \partial_{k_x} u_j(\mathbf{k}) \left| \partial_{k_y} u_j(\mathbf{k}) \right\rangle - \left\langle \partial_{k_y} u_j(\mathbf{k}) \right| \partial_{k_x} u_j(\mathbf{k}) \rangle . \tag{D2}$$

Inserting the identity operator $\sum_r |u_r(\mathbf{k})\rangle \langle u_r(\mathbf{k})|$ into Eq. (D2) further yields

$$\begin{aligned} F_{xy}^{(j)} &= \sum_r \langle \partial_{k_x} u_j(\mathbf{k}) \, |u_r(\mathbf{k})\rangle \langle u_r(\mathbf{k}) \, \left|\partial_{k_y} u_j(\mathbf{k})\right\rangle \\ &\quad - \left\langle \partial_{k_y} u_j(\mathbf{k})\right| \, u_r(\mathbf{k})\rangle \langle u_r(\mathbf{k})| \, \partial_{k_x} u_j(\mathbf{k})\rangle \\ &= \sum_{r\neq j} \langle \partial_{k_x} u_j(\mathbf{k}) \, |u_r(\mathbf{k})\rangle \langle u_r(\mathbf{k}) \, \left|\partial_{k_y} u_j(\mathbf{k})\right\rangle \\ &\quad - \left\langle \partial_{k_y} u_j(\mathbf{k})\right| \, u_r(\mathbf{k})\rangle \langle u_r(\mathbf{k})| \, \partial_{k_x} u_j(\mathbf{k})\rangle . \end{aligned} \tag{D3}$$

where the terms with $r = j$ can be verified to vanish.

On the other hand, we note that for $r \neq j$, there should be

$$\begin{aligned} &\langle u_j(\mathbf{k})| \nabla_{\mathbf{k}} h(\mathbf{k}) |u_r(\mathbf{k})\rangle \\ =& \langle u_j(\mathbf{k})| \nabla_{\mathbf{k}} \left(h(\mathbf{k}) |u_r(\mathbf{k})\rangle\right) - \langle u_j(\mathbf{k})| h(\mathbf{k}) |\nabla_{\mathbf{k}} u_r(\mathbf{k})\rangle \\ =& \langle u_j(\mathbf{k})| \nabla_{\mathbf{k}} \left(E_r(\mathbf{k}) \, u_r(\mathbf{k})\right) - E_j(\mathbf{k}) \langle u_j(\mathbf{k})| \nabla_{\mathbf{k}} u_r(\mathbf{k})\rangle \\ =& \nabla_{\mathbf{k}} E_r(\mathbf{k}) \langle u_j(\mathbf{k})| \, u_r(\mathbf{k})\rangle + E_r(\mathbf{k}) \langle u_j(\mathbf{k})| \nabla_{\mathbf{k}} u_r(\mathbf{k})\rangle \\ &- E_j(\mathbf{k}) \langle u_j(\mathbf{k})| \nabla_{\mathbf{k}} u_r(\mathbf{k})\rangle \\ =& \left(E_r(\mathbf{k}) - E_j(\mathbf{k})\right) \langle u_j(\mathbf{k}) \, |\nabla_{\mathbf{k}} u_r(\mathbf{k})\rangle , \end{aligned} \tag{D4}$$

where the gradient operator $\nabla_{\mathbf{k}} = \mathbf{e}_x \partial_{k_x} + \mathbf{e}_y \partial_{k_y}$, the orthogonal relation $\langle u_j(\mathbf{k})| \, u_r(\mathbf{k})\rangle = 0$ has been used and the result

$$\langle u_j(\mathbf{k}) \, |\nabla_{\mathbf{k}} u_r(\mathbf{k})\rangle = \frac{\langle u_j(\mathbf{k})| \nabla_{\mathbf{k}} h(\mathbf{k}) |u_r(\mathbf{k})\rangle}{E_r(\mathbf{k}) - E_j(\mathbf{k})} \tag{D5}$$

can hence be obtained.

Having obtained Eq. (D5), Eq. (D3) can then be transformed into

$$\begin{aligned} F_{xy}^{(j)} &= \langle \partial_{k_x} u_j(\mathbf{k}) \left| \partial_{k_y} u_j(\mathbf{k}) \right\rangle - \left\langle \partial_{k_y} u_j(\mathbf{k}) \right| \partial_{k_x} u_j(\mathbf{k}) \rangle \\ &= \sum_{r \neq j} \frac{\langle u_j | \partial_{k_x} h(\mathbf{k}) | u_r \rangle \langle u_r | \partial_{k_y} h(\mathbf{k}) | u_j \rangle}{\left[E_j(\mathbf{k}) - E_r(\mathbf{k})\right]^2} \\ &\quad - \frac{\langle u_j | \partial_{k_y} h(\mathbf{k}) | u_r \rangle \langle u_r | \partial_{k_x} h(\mathbf{k}) | u_j \rangle}{\left[E_j(\mathbf{k}) - E_r(\mathbf{k})\right]^2}. \end{aligned} \tag{D6}$$

We can see from Eq. (D6) that a peak or dip can occur where the jth band $E_j(\mathbf{k})$ greatly approaches its adjacent band $E_{j\pm1}(\mathbf{k})$.

Appendix E: Hofstadter-butterfly spectrum measurement

Here, we give details on how to calculate $\chi_{nm}(t) = 2\langle \sigma_{nm}^{+}(t) \rangle$, which represents the evolution of the single-qubit raising operator. In Sec. III B, we have introduced single-particle eigenstate creation operator [see Eq. (25)], which is

$$S_j^{+} = |E_j\rangle\langle 0| = \sum_{n=-N}^{N} \sum_{m=-M}^{M} \psi_{nm}^{(j)} \sigma_{nm}^{+} \tag{E1}$$

considering $\sigma_{nm}^{+} \equiv a_{nm}^{\dagger}$ in the single-particle regime. The completeness relation $\sum_j \psi_{nm}^{(j)} \psi_{n'm'}^{(j)*} = \delta_{nm,n'm'}$ further gives

$$\sigma_{nm}^{+} = \sum_{j=1}^{LW} \psi_{nm}^{(j)*} S_j^{+}. \tag{E2}$$

Subject to the Harper Hamiltonian [see Eq. (20)], the single-qubit raising operator after time t becomes

$$\begin{aligned} \sigma_{nm}^{+}(t) &= \sum_{j=1}^{LW} \psi_{nm}^{(j)*} S_j^{+} e^{i\frac{E_j}{\hbar}t} \\ &= \sum_{j=1}^{LW} \psi_{nm}^{(j)*} \sum_{n'=-N}^{N} \sum_{m'=-M}^{M} \psi_{n'm'}^{(j)} \sigma_{n'm'}^{+} e^{i\frac{E_j}{\hbar}t} \\ &= \sum_{n'=-N}^{N} \sum_{m'=-M}^{M} \sum_{j=1}^{LW} \psi_{nm}^{(j)*} \psi_{n'm'}^{(j)} \sigma_{n'm'}^{+} e^{i\frac{E_j}{\hbar}t}. \end{aligned} \tag{E3}$$

For the initial state $(|0\rangle + |1_{nm}\rangle)/\sqrt{2}$, the time evolution of the raising operator σ_{nm}^{+} can be quantified by

$$\chi_{nm}(t) = 2\left\langle \sigma_{nm}^{+}(t) \right\rangle = \sum_{j=1}^{LW} \left| \psi_{nm}^{(j)} \right|^2 e^{i\frac{E_j}{\hbar}t}. \tag{E4}$$

When averaging χ_{nm} over all the sites, we can then obtain

$$\begin{aligned} \bar{\chi}(t) &= \frac{1}{LW} \sum_{n=-N}^{N} \sum_{m=-M}^{M} \chi_{nm}(t) \\ &= \frac{1}{LW} \sum_{n=-N}^{N} \sum_{m=-M}^{M} \sum_{j=1}^{LW} \left| \psi_{nm}^{(j)} \right|^2 e^{i\frac{E_j}{\hbar}t} \\ &= \frac{1}{LW} \sum_{j=1}^{LW} \left(\sum_{n=-N}^{N} \sum_{m=-M}^{M} \left| \psi_{nm}^{(j)} \right|^2 \right) e^{i\frac{E_j}{\hbar}t} \\ &= \frac{1}{LW} \sum_{j=1}^{LW} e^{i\frac{E_j}{\hbar}t}, \end{aligned} \tag{E5}$$

from which, we can see the frequencies that occur in the Fourier transformation of $\chi(t)$, with a homogeneous amplitude $\frac{1}{LW}$, are the eigen energies of the Harper Hamiltonian.

Besides, we point out that the Hofstadter-butterfly spectrum can also be constructed via measuring the time-dependent wave function through subsequently exciting all the qubits (see Appendix. V E).

[1] P. Krantz, M. Kjaergaard, F. Yan, T. P. Orlando, S. Gustavsson, and W. D. Oliver, A quantum engineer's guide to superconducting qubits, Appl. Phys. Rev. **6**, 021318 (2019).

[2] R. Barends, J. Kelly, A. Megrant, A. Veitia, D. Sank, E. Jeffrey, T. C. White, J. Mutus, A. G. Fowler, B. Campbell, Y. Chen, Z. Chen, B. Chiaro, A. Dunsworth, C. Neill, P. O'Malley, P. Roushan, A. Vainsencher, J. Wenner, A. N. Korotkov, A. N. Cleland, and J. M. Martinis, Superconducting quantum circuits at the surface code threshold for fault tolerance, Nature **508**, 500 (2014).

[3] J. M. Chow, J. M. Gambetta, E. Magesan, D. W. Abraham, A. W. Cross, B. R. Johnson, N. A. Masluk, C. A. Ryan, J. A. Smolin, S. J. Srinivasan, and M. Steffen, Implementing a strand of a scalable fault-tolerant quantum computing fabric, Nat. Commun. **5**, 4015 (2014).

[4] M. Gong, X. Yuan, S. Wang, Y. Wu, Y. Zhao, C. Zha, S. Li, Z. Zhang, Q. Zhao, Y. Liu, F. Liang, J. Lin, Y. Xu, H. Deng, H. Rong, H. Lu, S. C. Benjamin, C.-Z. Peng, X. Ma, Y.-A. Chen, X. Zhu, and J.-W. Pan, Experimental exploration of five-qubit quantum error-correcting code with superconducting qubits, Natl. Sci. Rev. **9**, nwab011 (2022).

[5] F. Arute, K. Arya, R. Babbush, D. Bacon, J. C. Bardin, R. Barends, R. Biswas, S. Boixo, F. G. S. L. Brandao, D. A. Buell, B. Burkett, Y. Chen, Z. Chen, B. Chiaro, R. Collins, W. Courtney, A. Dunsworth, E. Farhi, B. Foxen, A. Fowler, C. Gidney, M. Giustina, R. Graff, K. Guerin, S. Habegger, M. P. Harrigan, M. J. Hartmann, A. Ho, M. Hoffmann, T. Huang, T. S. Humble, S. V. Isakov, E. Jeffrey, Z. Jiang, D. Kafri, K. Kechedzhi, J. Kelly, P. V. Klimov, S. Knysh, A. Korotkov, F. Kostritsa, D. Landhuis, M. Lindmark, E. Lucero, D. Lyakh, S. Mandra, J.

R. McClean, M. McEwen, A. Megrant, X. Mi, K. Michielsen, M. Mohseni, J. Mutus, O. Naaman, M. Neeley, C. Neill, M. Y. Niu, E. Ostby, A. Petukhov, J. C. Platt, C. Quintana, E. G. Rieffel, P. Roushan, N. C. Rubin, D. Sank, K. J. Satzinger, V. Smelyanskiy, K. J. Sung, M. D. Trevithick, A. Vainsencher, B. Villalonga, T. White, Z. J. Yao, P. Yeh, A. Zalcman, H. Neven, and J. M. Martinis, Quantum supremacy using a programmable superconducting processor, Nature **574**, 505 (2019).

[6] Y. L. Wu, W. S. Bao, S. R. Cao, F. S. Chen, M. C. Chen, X. W. Chen, T. H. Chung, H. Deng, Y. J. Du, D. J. Fan, M. Gong, C. Guo, C. Guo, S. J. Guo, L. C. Han, L. Y. Hong, H. L. Huang, Y. H. Huo, L. P. Li, N. Li, S. W. Li, Y. Li, F. T. Liang, C. Lin, J. Lin, H. R. Qian, D. Qiao, H. Rong, H. Su, L. H. Sun, L. Y. Wang, S. Y. Wang, D. C. Wu, Y. Xu, K. Yan, W. F. Yang, Y. Yang, Y. S. Ye, J. H. Yin, C. Ying, J. L. Yu, C. Zha, C. Zhang, H. B. Zhang, K. L. Zhang, Y. M. Zhang, H. Zhao, Y. W. Zhao, L. Zhou, Q. L. Zhu, C. Y. Lu, C. Z. Peng, X. B. Zhu, and J. W. Pan, Strong Quantum Computational Advantage Using a Superconducting Quantum Processor, Phys. Rev. Lett. **127**, 180501 (2021).

[7] Q. L. Zhu, S. R. Cao, F. S. Chen, M. C. Chen, X. W. Chen, T. H. Chung, H. Deng, Y. J. Du, D. J. Fan, M. Gong, C. Guo, C. Guo, S. J. Guo, L. C. Han, L. Y. Hong, H. L. Huang, Y. H. Huo, L. P. Li, N. Li, S. W. Li, Y. Li, F. T. Liang, C. Lin, J. Lin, H. R. Qian, D. Qiao, H. Rong, H. Su, L. H. Sun, L. Y. Wang, S. Y. Wang, D. C. Wu, Y. L. Wu, Y. Xu, K. Yan, W. F. Yang, Y. Yang, Y. Ye, J. H. Yin, C. Ying, J. L. Yu, C. Zha, C. Zhang, H. B. Zhang, K. L. Zhang, Y. M. Zhang, H. Zhao, Y. W. Zhao, L. Zhou, C. Y. Lu, C. Z. Peng, X. B. Zhu, and J. W. Pan, Quantum computational advantage via 60-qubit 24-cycle random circuit sampling, Sci. Bull. **67**, 240 (2022).

[8] P. J. J. O'Malley, R. Babbush, I. D. Kivlichan, J. Romero, J. R. McClean, R. Barends, J. Kelly, P. Roushan, A. Tranter, N. Ding, B. Campbell, Y. Chen, Z. Chen, B. Chiaro, A. Dunsworth, A. G. Fowler, E. Jeffrey, E. Lucero, A. Megrant, J. Y. Mutus, M. Neeley, C. Neill, C. Quintana, D. Sank, A. Vainsencher, J. Wenner, T. C. White, P. V. Coveney, P. J. Love, H. Neven, A. Aspuru-Guzik, and J. M. Martinis, Scalable Quantum Simulation of Molecular Energies, Phys. Rev. X **6,** 031007 (2016).

[9] A. Kandala, A. Mezzacapo, K. Temme, M. Takita, M. Brink, J. M. Chow, and J. M. Gambetta, Hardware-efficient variational quantum eigensolver for small molecules and quantum magnets, Nature **549**, 242 (2017).

[10] F. Arute, K. Arya, R. Babbush, D. Bacon, C. Bardin Joseph, R. Barends, S. Boixo, M. Broughton, B. Buckley Bob, A. Buell David, B. Burkett, N. Bushnell, Y. Chen, Z. Chen, B. Chiaro, R. Collins, W. Courtney, S. Demura, A. Dunsworth, E. Farhi, A. Fowler, B. Foxen, C. Gidney, M. Giustina, R. Graff, S. Habegger, P. Harrigan Matthew, A. Ho, S. Hong, T. Huang, J. Huggins William, L. Ioffe, V. Isakov Sergei, E. Jeffrey, Z. Jiang, C. Jones, D. Kafri, K. Kechedzhi, J. Kelly, S. Kim, V. Klimov Paul, A. Korotkov, F. Kostritsa, D. Landhuis, P. Laptev, M. Lindmark, E. Lucero, O. Martin, M. Martinis John, R. McClean Jarrod, M. McEwen, A. Megrant, X. Mi, M. Mohseni, W. Mruczkiewicz, J. Mutus, O. Naaman, M. Neeley, C. Neill, H. Neven, Y. Niu Murphy, E. O'Brien Thomas, E. Ostby, A. Petukhov, H. Putterman, C. Quintana, P. Roushan, C. Rubin Nicholas, D. Sank, J. Satzinger Kevin, V. Smelyanskiy, D. Strain, J. Sung Kevin, M. Szalay, Y. Takeshita Tyler, A. Vainsencher, T. White, N. Wiebe, Z. J. Yao, P. Yeh, and A. Zalcman, Hartree-Fock on a superconducting qubit quantum computer, Science **369**, 1084 (2020).

[11] J. Chow, O. Dial, and J. Gambetta, IBM Quantum breaks the 100-qubit processor barrier, (IBM) https://research.ibm.com/blog/127-qubit-quantum-processor-eagle (Accessed 16 Nov 2021).

[12] A. P. M. Place, L. V. H. Rodgers, P. Mundada, B. M. Smitham, M. Fitzpatrick, Z. Leng, A. Premkumar, J. Bryon, A. Vrajitoarea, S. Sussman, G. Cheng, T. Madhavan, H. K. Babla, X. H. Le, Y. Gang, B. Jack, A. Gyenis, N. Yao, R. J. Cava, N. P. de Leon, and A. A. Houck, New material platform for superconducting transmon qubits with coherence times exceeding 0.3 milliseconds, Nat. Commun. **12**, 1779 (2021).

[13] C. Wang, X. Li, H. Xu, Z. Li, J. Wang, Z. Yang, Z. Mi, X. Liang, T. Su, C. Yang, G. Wang, W. Wang, Y. Li, M. Chen, C. Li, K. Linghu, J. Han, Y. Zhang, Y. Feng, Y. Song, T. Ma, J. Zhang, R. Wang, P. Zhao, W. Liu, G. Xue, Y. Jin, and H. Yu, Towards practical quantum computers: transmon qubit with a lifetime approaching 0.5 milliseconds, npj Quantum. Inform. **8**, 3 (2022).

[14] J. Preskill, Quantum Computing, Quantum **2**, 79 (2018).

[15] M. Kjaergaard, M. E. Schwartz, J. Braumuller, P. Krantz, J. I. J. Wang, S. Gustavsson, and W. D. Oliver, Superconducting Qubits: Current State of Play, Annu. Rev. Condens. Matter Phys. **11**, 369 (2020).

[16] P. J. Leek, J. M. Fink, A. Blais, R. Bianchetti, M. Göppl, J. M. Gambetta, D. I. Schuster, L. Frunzio, R. J. Schoelkopf, and A. Wallraff, Observation of Berry's Phase in a Solid-State Qubit, Science **318**, 1889 (2007).

[17] S. Berger, M. Pechal, S. Pugnetti, A. A. Abdumalikov, L. Steffen, A. Fedorov, A. Wallraff, and S. Filipp, Geometric phases in superconducting qubits beyond the two-level approximation, Phys. Rev. B **85**, 220502(R) (2012).

[18] S. Berger, M. Pechal, A. A. Abdumalikov, C. Eichler, L. Steffen, A. Fedorov, A. Wallraff, and S. Filipp, Exploring the effect of noise on the Berry phase, Phys. Rev. A **87**, 060303(R) (2013).

[19] M. D. Schroer, M. H. Kolodrubetz, W. F. Kindel, M. Sandberg, J. Gao, M. R. Vissers, D. P. Pappas, A. Polkovnikov, and K. W. Lehnert, Measuring a topological transition in an artificial spin-1/2 system, Phys. Rev. Lett. **113**, 050402 (2014).

[20] Z. Zhang, T. Wang, L. Xiang, J. Yao, J. Wu, and Y. Yin, Measuring the Berry phase in a superconducting phase qubit by a shortcut to adiabaticity, Phys. Rev. A **95**, 042345 (2017).

[21] P. Roushan, C. Neill, Y. Chen, M. Kolodrubetz, C. Quintana, N. Leung, M. Fang, R. Barends, B. Campbell, Z. Chen, B. Chiaro, A. Dunsworth, E. Jeffrey, J. Kelly, A. Megrant, J. Mutus, P. J. O'Malley, D. Sank, A. Vainsencher, J. Wenner, T. White, A. Polkovnikov, A. N. Cleland, and J. M. Martinis, Observation of topological transitions in interacting quantum circuits, Nature **515**, 241 (2014).

[22] E. Flurin, V. V. Ramasesh, S. Hacohen-Gourgy, L. S. Martin, N. Y. Yao, and I. Siddiqi, Observing Topological Invariants Using Quantum Walks in Superconducting Circuits, Phys. Rev. X **7**, 031023 (2017).

[23] V. V. Ramasesh, E. Flurin, M. Rudner, I. Siddiqi, and N. Y. Yao, Direct Probe of Topological Invariants Using Bloch Oscillating Quantum Walks, Phys. Rev. Lett. **118**, 130501 (2017).

[24] X. Tan, Y. Zhao, Q. Liu, G. Xue, H. Yu, Z. D. Wang, and Y. Yu, Realizing and manipulating space-time inversion symmetric topological semimetal bands with superconducting quantum circuits, npj Quantum Materials **2**, 60 (2017).

[25] X. Tan, D. W. Zhang, Q. Liu, G. Xue, H. F. Yu, Y. Q. Zhu, H. Yan, S. L. Zhu, and Y. Yu, Topological Maxwell Metal Bands in a Superconducting Qutrit, Phys. Rev. Lett. **120**, 130503 (2018).

[26] Y. P. Zhong, D. Xu, P. Wang, C. Song, Q. J. Guo, W. X. Liu, K. Xu, B. X. Xia, C. Y. Lu, S. Han, J. W. Pan, and H. Wang, Emulating Anyonic Fractional Statistical Behavior in a Superconducting Quantum Circuit, Phys. Rev. Lett. **117**, 110501 (2016).

[27] X.-Y. Guo, C. Yang, Y. Zeng, Y. Peng, H.-K. Li, H. Deng, Y.-R.

Jin, S. Chen, D. Zheng, and H. Fan, Observation of a Dynamical Quantum Phase Transition by a Superconducting Qubit Simulation, Phys. Rev. Applied **11**, 044080 (2019).

[28] A. Nunnenkamp, J. Koch, and S. M. Girvin, Synthetic Gauge Fields and Homodyne Transmission in Jaynes-Cummings Lattices, New J. Phys. **13**, 095008 (2011).

[29] F. Mei, J.-B. You, W. Nie, R. Fazio, S.-L. Zhu, and L. C. Kwek, Simulation and detection of photonic Chern insulators in a one-dimensional circuit-QED lattice, Phys. Rev. A **92**, 041805(R) (2015).

[30] Z.-H. Yang, Y.-P. Wang, Z.-Y. Xue, W.-L. Yang, Y. Hu, J.-H. Gao, and Y. Wu, Circuit Quantum Electrodynamics Simulator of Flat Band Physics in a Lieb Lattice, Phys. Rev. A **93**, 062319 (2016).

[31] J. Tangpanitanon, V. M. Bastidas, S. Al-Assam, P. Roushan, D. Jaksch, and D. G. Angelakis, Topological Pumping of Photons in Nonlinear Resonator Arrays, Phys. Rev. Lett. **117**, 213603 (2016).

[32] X. Gu, S. Chen, and Y. Liu, Topological edge states and pumping in a chain of coupled superconducting qubits, arXiv:1711.06829v1 [quant-ph] (2017).

[33] W. Nie, M. Antezza, Y. X. Liu, and F. Nori, Dissipative Topological Phase Transition with Strong System-Environment Coupling, Phys. Rev. Lett. 127, 250402 (2021).

[34] Y. Zhang, W. Nie, and Y.-x. Liu, Edge-State Oscillations in a One-Dimensional Topological Chain with Dissipative Couplings, Phys. Rev. Applied 18,024038 (2022).

[35] P. Roushan, C. Neill, J. Tangpanitanon, V. M. Bastidas, A. Megrant, R. Barends, Y. Chen, Z. Chen, B. Chiaro, A. Dunsworth, A. Fowler, B. Foxen, M. Giustina, E. Jeffrey, J. Kelly, E. Lucero, J. Mutus, M. Neeley, C. Quintana, D. Sank, A. Vainsencher, J. Wenner, T. White, H. Neven, D. G. Angelakis, and J. Martinis, Spectroscopic Signatures of Localization with Interacting Photons in Superconducting Qubits, Science 358, 1175 (2017).

[36] P. Roushan, C. Neill, A. Megrant, Y. Chen, R. Babbush, R. Barends, B. Campbell, Z. Chen, B. Chiaro, A. Dunsworth, A. Fowler, E. Jeffrey, J. Kelly, E. Lucero, J. Mutus, P. J. J. O'Malley, M. Neeley, C. Quintana, D. Sank, A. Vainsencher, J. Wenner, T. White, E. Kapit, H. Neven, and J. Martinis, Chiral Ground-State Currents of Interacting Photons in a Synthetic Magnetic Field, Nat. Phys. **13**, 146 (2017).

[37] K. Xu, J.-J. Chen, Y. Zeng, Y.-R. Zhang, C. Song, W. Liu, Q. Guo, P. Zhang, D. Xu, H. Deng, K. Huang, H. Wang, X. Zhu, D. Zheng, and H. Fan, Emulating Many-Body Localization with a Superconducting Quantum Processor, Phys. Rev. Lett. 120, 050507 (2018).

[38] Z. Yan, Y.-R. Zhang, M. Gong, Y. Wu, Y. Zheng, S. Li, C. Wang, F. Liang, J. Lin, Y. Xu, C. Guo, L. Sun, C.-Z. Peng, K. Xia, H. Deng, H. Rong, J. Q. You, F. Nori, H. Fan, X. Zhu, and J.-W. Pan, Strongly Correlated Quantum Walks with a 12-Qubit Superconducting Processor, Science **364**, 753 (2019).

[39] Y. Ye, Z.-Y. Ge, Y. Wu, S. Wang, M. Gong, Y.-R. Zhang, Q. Zhu, R. Yang, S. Li, F. Liang, J. Lin, Y. Xu, C. Guo, L. Sun, C. Cheng, N. Ma, Z. Y. Meng, H. Deng, H. Rong, C.-Y. Lu, C.-Z. Peng, H. Fan, X. Zhu, and J.-W. Pan, Propagation and Localization of Collective Excitations on a 24-Qubit Superconducting Processor, Phys. Rev. Lett. **123**, 050502 (2019).

[40] Y.-J. Zhao, X.-W. Xu, H. Wang, Y.-x. Liu, and W.-M. Liu, Vortex-Meissner Phase Transition Induced by a Two-Tone-Drive-Engineered Artificial Gauge Potential in the Fermionic Ladder Constructed by Superconducting Qubit Circuits, Phys. Rev. A **102**, 053722 (2020).

[41] X. Guan, Y. Feng, Z.-Y. Xue, G. Chen, and S. Jia, Synthetic Gauge Field and Chiral Physics on Two-Leg Superconducting Circuits, Phys. Rev. A **102**, 032610 (2020).

[42] R.-C. Ge and M. Kolodrubetz, Floquet Engineering Flat Bands for Bosonic Fractional Quantum Hall with Superconducting Circuits, Phys. Rev. B **104**, 035427 (2021).

[43] X. Mi, M. Ippoliti, C. Quintana, A. Greene, Z. Chen, J. Gross, F. Arute, K. Arya, J. Atalaya, R. Babbush, J. C. Bardin, J. Basso, A. Bengtsson, A. Bilmes, A. Bourassa, L. Brill, M. Broughton, B. B. Buckley, D. A. Buell, B. Burkett, N. Bushnell, B. Chiaro, R. Collins, W. Courtney, D. Debroy, S. Demura, A. R. Derk, A. Dunsworth, D. Eppens, C. Erickson, E. Farhi, A. G. Fowler, B. Foxen, C. Gidney, M. Giustina, M. P. Harrigan, S. D. Harrington, J. Hilton, A. Ho, S. Hong, T. Huang, A. Huff, W. J. Huggins, L. B. Ioffe, S. V. Isakov, J. Iveland, E. Jeffrey, Z. Jiang, C. Jones, D. Kafri, T. Khattar, S. Kim, A. Kitaev, P. V. Klimov, A. N. Korotkov, F. Kostritsa, D. Landhuis, P. Laptev, J. Lee, K. Lee, A. Locharla, E. Lucero, O. Martin, J. R. McClean, T. McCourt, M. McEwen, K. C. Miao, M. Mohseni, S. Montazeri, W. Mruczkiewicz, O. Naaman, M. Neeley, C. Neill, M. Newman, M. Y. Niu, T. E. O'Brien, A. Opremcak, E. Ostby, B. Pato, A. Petukhov, N. C. Rubin, D. Sank, K. J. Satzinger, V. Shvarts, Y. Su, D. Strain, M. Szalay, M. D. Trevithick, B. Villalonga, T. White, Z. J. Yao, P. Yeh, J. Yoo, A. Zalcman, H. Neven, S. Boixo, V. Smelyanskiy, A. Megrant, J. Kelly, Y. Chen, S. L. Sondhi, R. Moessner, K. Kechedzhi, V. Khemani and P. Roushan, Time-crystalline eigenstate order on a quantum processor, Nature **601**, 531 (2021).

[44] Y. Hatsugai, Chern number and edge states in the integer quantum Hall effect, Phys. Rev. Lett. **71**, 3697 (1993).

[45] Y. Hatsugai, Edge States in the Integer Quantum Hall Effect and the Riemann Surface of the Bloch Function, Phys. Rev. B **48**, 11851 (1993).

[46] M. Aidelsburger, M. Atala, S. Nascimbène, S. Trotzky, Y. A. Chen, and I. Bloch, Experimental Realization of Strong Effective Magnetic Fields in an Optical Lattice, Phys. Rev. Lett. **107**, 255301 (2011).

[47] M. Aidelsburger, M. Atala, M. Lohse, J. T. Barreiro, B. Paredes, and I. Bloch, Realization of the Hofstadter Hamiltonian with Ultracold Atoms in Optical Lattices, Phys. Rev. Lett. **111**, 185301 (2013).

[48] H. Miyake, G. A. Siviloglou, C. J. Kennedy, W. C. Burton, and W. Ketterle, Realizing the Harper Hamiltonian with Laser-Assisted Tunneling in Optical Lattices, Phys. Rev. Lett. **111**, 185302 (2013).

[49] A. Celi, P. Massignan, J. Ruseckas, N. Goldman, I. B. Spielman, G. Juzeliunas, and M. Lewenstein, Synthetic Gauge Fields in Synthetic Dimensions, Phys. Rev. Lett. **112**, 043001 (2014).

[50] Y. Chen, C. Neill, P. Roushan, N. Leung, M. Fang, R. Barends, J. Kelly, B. Campbell, Z. Chen, B. Chiaro, A. Dunsworth, E. Jeffrey, A. Megrant, J. Y. Mutus, P. J. J. O'Malley, C. M. Quintana, D. Sank, A. Vainsencher, J. Wenner, T. C. White, M. R. Geller, A. N. Cleland, and J. M. Martinis, Qubit Architecture with High Coherence and Fast Tunable Coupling, Phys. Rev. Lett. **113**, 220502 (2014).

[51] J. Koch, A. A. Houck, K. L. Hur, and S. M. Girvin, Time-Reversal-Symmetry Breaking in Circuit-QED-Based Photon Lattices, Phys. Rev. A **82**, 043811 (2010).

[52] H. Alaeian, C. W. S. Chang, M. V. Moghaddam, C. M. Wilson, E. Solano, and E. Rico, Creating Lattice Gauge Potentials in Circuit Qed: The Bosonic Creutz Ladder, Phys. Rev. A **99**, 053834 (2019).

[53] T. Fukui, Y. Hatsugai, and H. Suzuki, Chern Numbers in Discretized Brillouin Zone: Efficient Method of Computing (Spin) Hall Conductances, J. Phys. Soc. Jpn. **74**, 1674 (2005).

[54] D. R. Hofstadter, Energy Levels and Wave Functions of Bloch Electrons in Rational and Irrational Magnetic Fields, Phys. Rev. B 14, 2239 (1976).

[55] M. Mancini, G. Pagano, G. Cappellini, L. Livi, M. Rider, J. Catani, C. Sias, P. Zoller, M. Inguscio, M. Dalmonte, and L. Fallani, Observation of Chiral Edge States with Neutral Fermions in Synthetic Hall Ribbons, Science **349**, 1510 (2015).

[56] J. Koch, T. Yu, J. Gambetta, A. Houck, D. Schuster, J. Majer, A. Blais, M. Devoret, S. Girvin, and R. Schoelkopf, Charge-Insensitive Qubit Design Derived from the Cooper Pair Box, Phys. Rev. A 76, 042319 (2007).

[57] M. Atala, M. Aidelsburger, M. Lohse, J. T. Barreiro, B. Paredes, and I. Bloch, Observation of chiral currents with ultracold atoms in bosonic ladders, Nat. Phys. **10**, 588 (2014).

[58] F. Mei, V. M. Stojanovic, I. Siddiqi, and L. Tian, Analog Superconducting Quantum Simulator for Holstein Polarons, Phys. Rev. B **88**, 224502 (2013).

[59] O. Derzhko, Jordan-Wigner Fermionization for Spin-1/2 Systems in Two Dimensions: A Brief Review, Journal of Physical Studies **5**, 49 (2001).

[60] B. A. Bernevig and L. H. Taylor, *Topological Insulators and Topological Superconductors*, (Princeton University Press, 2013).

[61] R. Barends, J. Kelly, A. Megrant, D. Sank, E. Jeffrey, Y. Chen, Y. Yin, B. Chiaro, J. Mutus, C. Neill, P. O?Malley, P. Roushan, J. Wenner, T. C. White, A. N. Cleland, and J. M. Martinis, Coherent Josephson Qubit Suitable for Scalable Quantum Integrated Circuits, Phys. Rev. Lett. **111**, 080502 (2013).

[62] M. R. Geller, E. Donate, Y. Chen, M. T. Fang, N. Leung, C. Neill, P. Roushan, and J. M. Martinis, Tunable coupler for superconducting Xmon qubits: Perturbative nonlinear model, Phys. Rev. A **92**, 012320 (2015).

[63] M. H. Devoret, Quantum fluctuations in electrical circuits, Les Houches, Session LXIII 7 (1995).